Corrosion Science 245 (2025) 112706

Contents lists available at ScienceDirect

Corrosion Science

journal homepage: www.elsevier.com/locate/corsci

A self-sealing and self-healing MAO corrosion-resistant coating on aluminum alloy by *in situ* growth of $CePO_4/Al_2O_3$

Chao Yang [a], Zongmin Sun [a], Chenyu Wang [a], Aihui Huang [b,*], Zishuo Ye [c], Tao Ying [a], Liping Zhou [a], Shu Xiao [c,*], Paul K. Chu [d,*], Xiaoqin Zeng [a]

[a] National Engineering Research Center of Light Alloy Net Forming, School of Materials Science and Engineering, Shanghai Jiao Tong University, Shanghai 200240, China
[b] Shanghai Key Laboratory of Advanced High-Temperature Materials and Precision Forming, School of Materials Science and Engineering, Shanghai Jiao Tong University, Shanghai 200240, China
[c] School of Mechanical & Automotive Engineering, South China University of Technology, Guangzhou 510641, China
[d] Department of Physics, Department of Materials Science & Engineering, and Department of Biomedical Engineering, City University of Hong Kong, Tat Chee Avenue, Kowloon 999077, Hong Kong

ARTICLE INFO

Keywords:
Aluminum alloy
Micro arc oxidation (MAO)
Self-sealing
Self-healing
Cerium phosphate
Corrosion resistance

ABSTRACT

A coating with self-sealing and self-healing properties is prepared on the LY12 aluminum alloy by microarc oxidation (MAO). The *in situ* growth of $CePO_4$ and Al_2O_3 creates a mixed melt that fills the discharge pores, while the mixed amorphous and nanocrystalline structure enhances the corrosion resistance. Electrochemical and saltwater immersion tests demonstrate that the Ce-doped MAO coating has excellent corrosion resistance without local pitting corrosion after immersion for 336 h. During immersion, $CePO_4$ releases Ce^{3+} to form $Ce(OH)_3$ to fill the loose corrosion product $Al(OH)_3$, consequently creating a denser product film with self-sealing and self-healing capabilities.

1. Introduction

Aluminum (Al) alloys have a wide range of applications in aerospace, marine equipment, automotive, and 3 C electronic components due to their low density, high strength, and easy processing [1–3]. However, components made of Al alloys are prone to corrosion in service [4–6], and protective coatings and subsequent painting treatments are commonly deposited for commercial applications [7,8]. Among them, the coating on the substrate surface includes anodizing, micro arc oxidation (MAO), etc., which are crucial for the corrosion resistance and wear resistance of the coating [9]. For instance, MAO produces an alumina layer *in situ* with enhanced corrosion resistance [10]. However, the arc discharge on the insulating layer produces pores on the surface [11,12] rendering the coating susceptible to the penetration of corrosive species through the pores to corrode the substrate during long-term use [13,14].

Generally, a secondary sealing process can reduce or prevent the permeation of corrosive medium through pores. Sealing techniques typically involve organic sealing and nanoparticle sealing [15,16]. In organic sealing, organic compounds such as epoxy resin, polyacrylamide, and so on are introduced into the MAO coating to cover the pores [17]. However, organic coatings may not adhere strongly to the substrate, giving rise to possible delamination, and also are susceptible to aging and failure [18]. In comparison, sealing with nanoparticles by MAO facilitates the aggregation and sealing of pores [19,20]. Nevertheless, nanoparticles tend to aggregate and precipitate in the electrolyte, leading to poor pore-sealing effects [21]. Therefore, it is important to modify the particles' surface charge thus making the process quite complex. Hence, precise control of the electrolyte is crucial [22,23]. Wu et al. have designed an electrolyte to prepare MAO coatings doped with zinc phosphate *in situ* on Al alloy [24]. During long-term corrosion, the surface zinc phosphate dissolves to release Zn^{2+} and form $Zn(OH)_2$ precipitate, which plays a self-healing role, and the neutral salt spraying lifetime is 5000 h. Dong et al. have prepared LDH films on MAO coatings on Mg alloys and integrated corrosion inhibitors and anchoring lubricants. The outermost sliding surface of the coating exhibits water resistance and self-healing ability, providing effective corrosion resistance [25]. However, in spite of self-healing, the risk of corrosion due to weak pores cannot be eliminated totally [26–32]. In this regard, Zhang et al. have constructed a composite MAO coating containing Ce to seal pores by exploiting the release of Ce^{3+}/Ce^{4+} during corrosion [33]. However, the bonding strength of the coating is still insufficient. It is

* Corresponding authors.
E-mail addresses: huangaihuivip@sjtu.edu.cn (A. Huang), xiaos@scut.edu.cn (S. Xiao), paul.chu@cityu.edu.hk (P.K. Chu).

https://doi.org/10.1016/j.corsci.2025.112706
Received 16 November 2024; Received in revised form 7 January 2025; Accepted 11 January 2025
Available online 13 January 2025

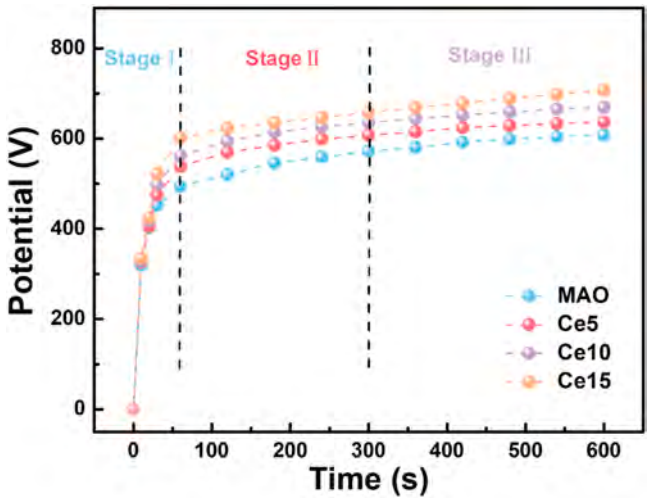

Fig. 1. Discharge curves during MAO of the LY12 Al alloy in the Ce-doped electrolytes.

desirable to develop a one-step process that can introduce both self-sealing and self-healing effects. In MAO, pores are formed by discharge breakdown and the subsequent reaction between the substrate and electrolyte to generate oxide and metal salts [34,35]. The local high temperature causes the reaction products to melt and solidify upon exposure to the cold electrolyte [36,37]. In this respect, if the molten materials can be enriched at the pores, they can, in principle, backfill the pores to accomplish *in situ* self-sealing.

In this study, Ce^{3+} with self-healing properties is introduced into a phosphate electrolyte to produce $CePO_4$-doped MAO coatings *in situ* on the LY12 Al alloy. The melt of $CePO_4$ and Al_2O_3 fills the pores. The coatings are characterized, and the corrosion characteristics are determined by immersion in a NaCl solution. The self-healing properties are investigated by introducing scratch damage and performing subsequent immersion studies.

2. Experimental section

2.1. Preparation of MAO coatings

The LY12 Al alloy ($50 \times 25 \times 1\ mm^3$) was polished with 2000 grit sandpaper and cleaned ultrasonically with deionized water and anhydrous ethanol for 10 min each. Microarc oxidation (MAO) was conducted in the constant current mode in an electrolyte doped with Ce^{3+} using a 15 kW AC power supply, with the Al alloy as the anode and the stainless-steel electrolytic cell as the cathode. The current density, frequency, duty cycle, and discharge time were $5\ A{\cdot}dm^{-2}$, 500 Hz, 15 %, and 10 minutes, respectively. The base electrolyte consisted of $15\ g{\cdot}L^{-1}$ $Na_4P_2O_7$, $5\ g{\cdot}L^{-1}$ NaOH, and $5\ g{\cdot}L^{-1}$ EDTA-2Na. The coatings were produced by adding $0/5/10/15\ g{\cdot}L^{-1}$ $Ce(CH_3CO_2)_3 \cdot xH_2O$ to the base electrolyte (samples designated as MAO, Ce5, Ce10, and Ce15, respectively). Cooling by circulating water was used to ensure that the temperature of the electrolyte was below 45 °C.

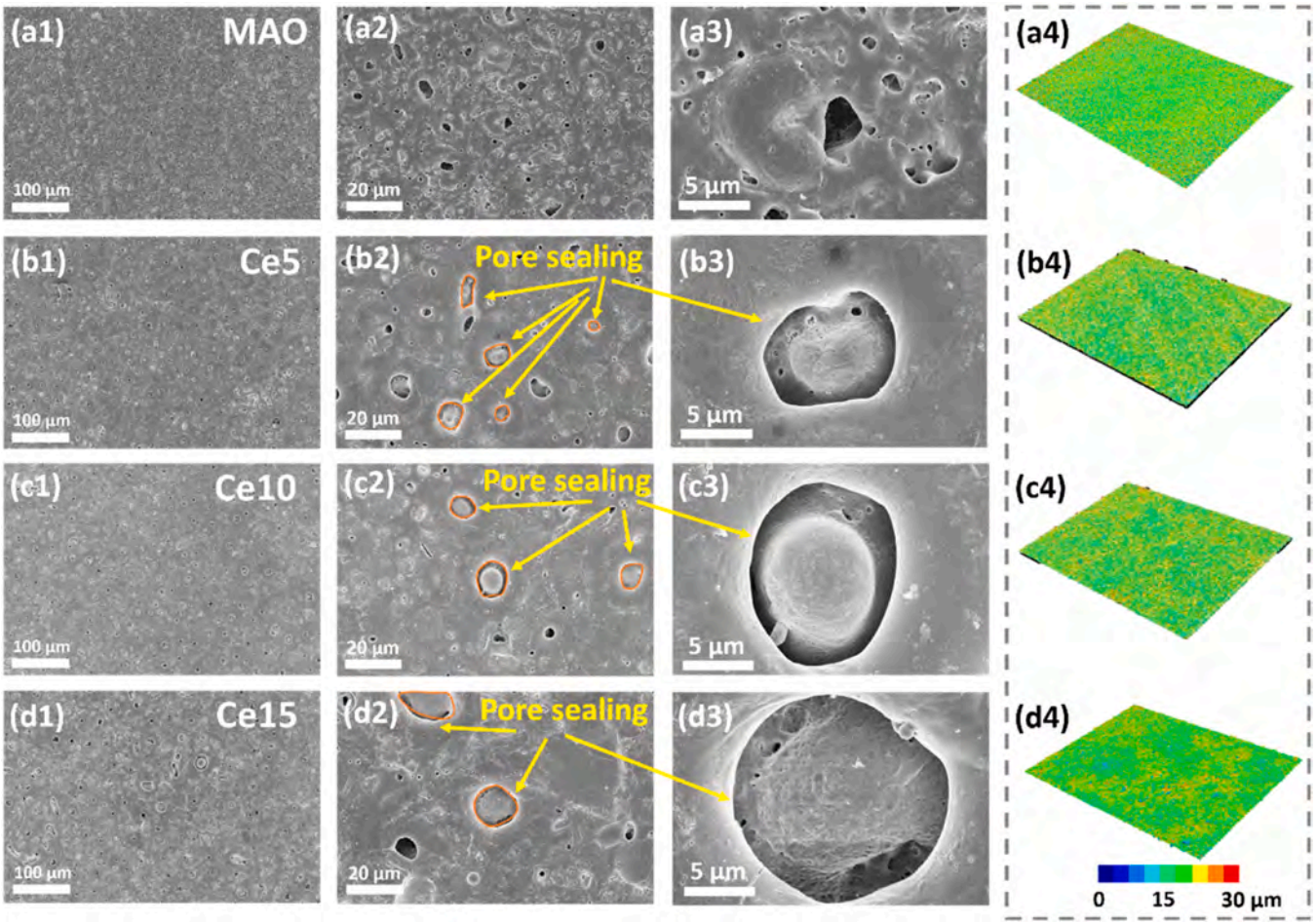

Fig. 2. SEM and LCSM images of the MAO coatings doped with different concentrations of Ce: (a) MAO, (b) Ce5, (c) Ce10, and (d) Ce15.

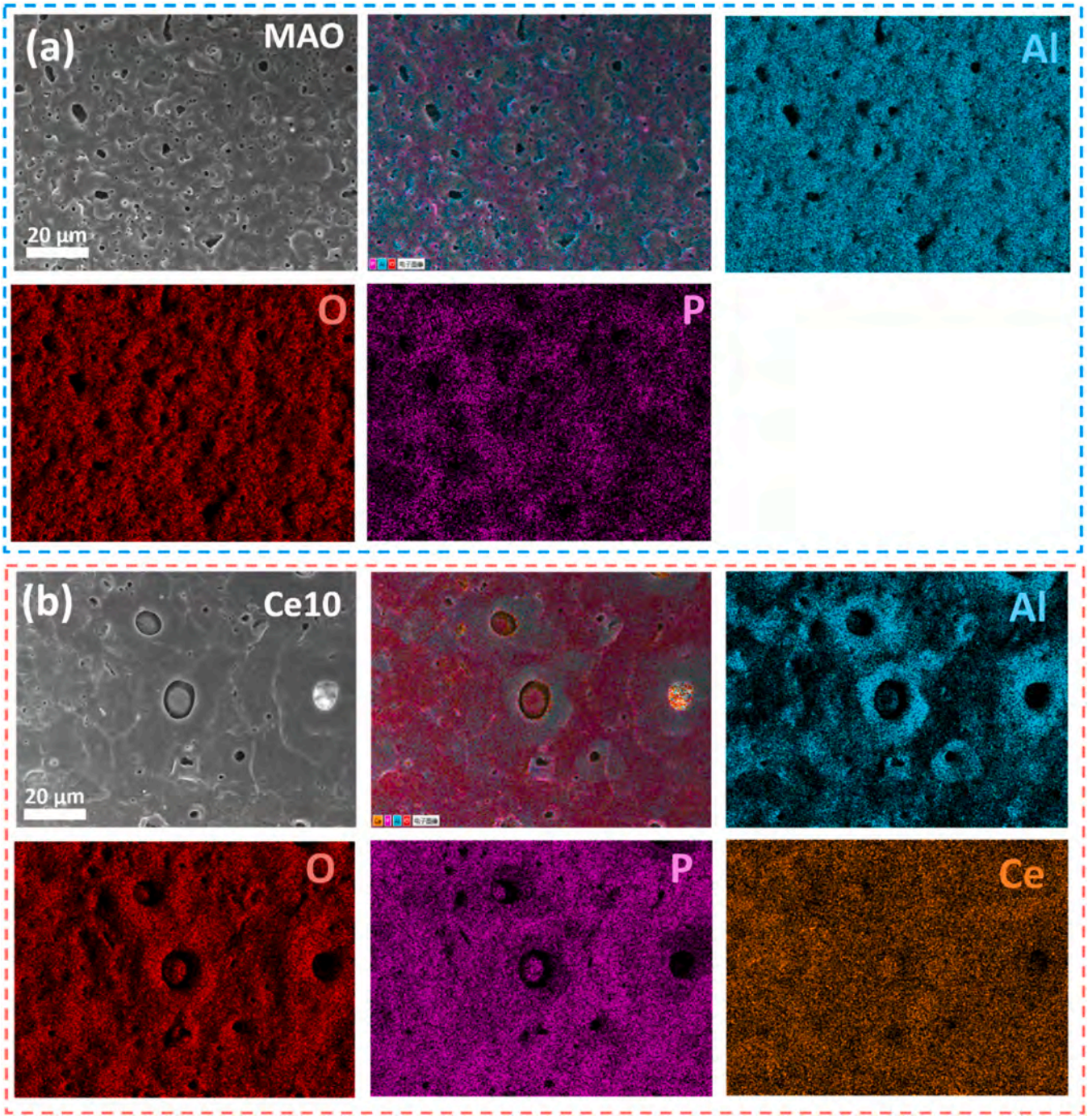

Fig. 3. SEM/EDS image and elemental maps: (a) MAO and (b) Ce10.

2.2. Electrochemical and immersion tests

Electrochemical and salt solution immersion tests were performed. The electrochemical evaluation was carried out on an electrochemical workstation (Gamry1010E) with a three-electrode configuration in a 3.5 wt% NaCl solution at room temperature, in which the sample, saturated calomel (SCE), and Pt were the working, reference, and counter electrodes, respectively. The sample was subjected to a 30-minute open circuit potential (OCP) operation in the solution for stabilization before electrochemical impedance spectroscopy (EIS) and polarization (Tafel) were conducted. EIS was carried out between 100 kHz and 100 mHz using a sinusoidal signal with an amplitude of 10 mV. The data were fitted and analyzed by ZsimpWin. The Tafel data were acquired by the dynamic potential test at a scanning rate of 1 $mV \cdot s^{-1}$, and the corrosion potential and corrosion current density were calculated by Tafel extrapolation. The salt solution corrosion experiment was conducted in a 3.5 wt% NaCl solution for 336 h. The samples were performed by a hundred grid scratch test and subjected to immersion tests to assess their self-healing properties. All the tests were done in triplicate to improve the statistics.

2.3. Characterization

The microstructure and corrosion product morphology of the MAO coatings were examined by scanning electron microscopy (SEM, Carl Zeiss, SUPRA55), and the elemental composition and distribution were

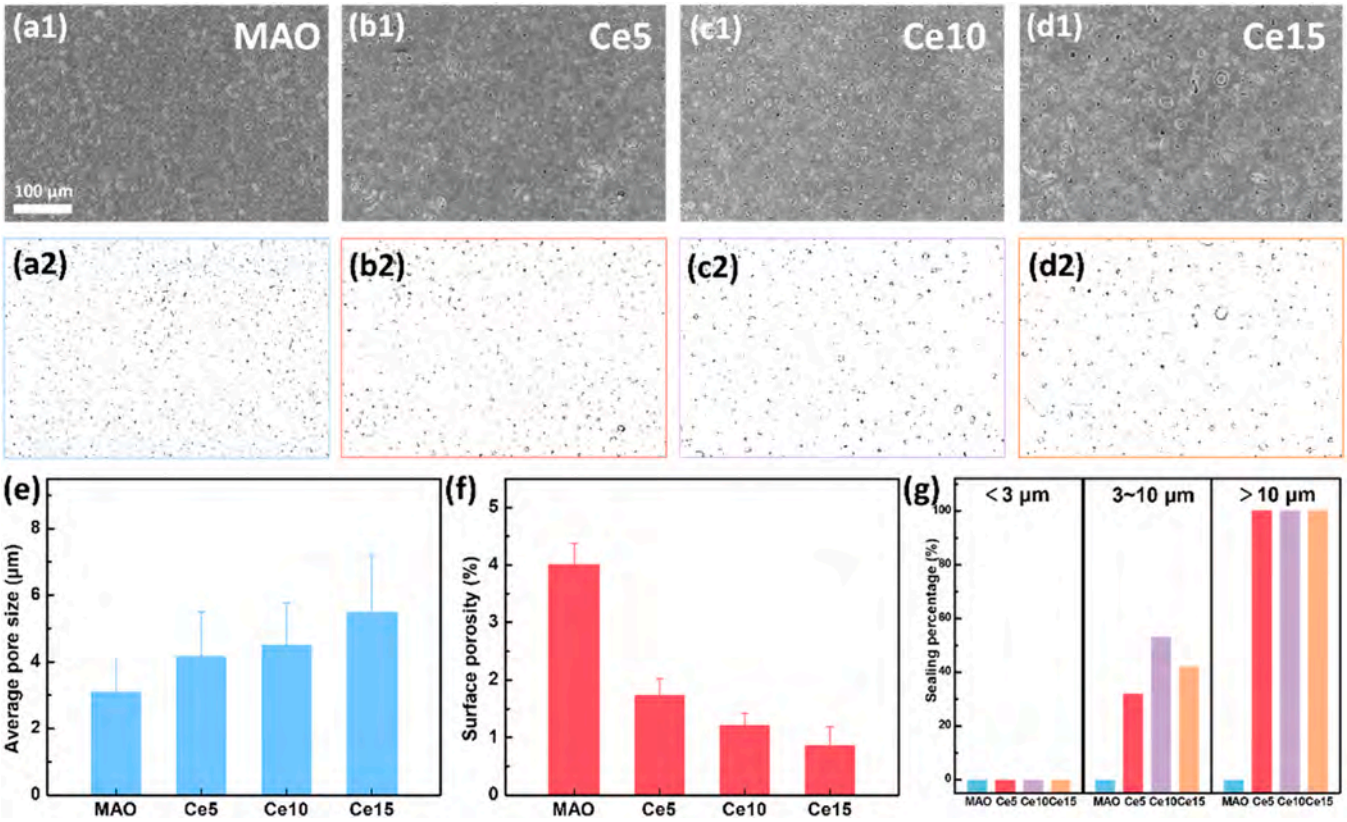

Fig. 4. Surface morphologies and corresponding micropore distributions of the MAO coatings: (a) MAO, (b) Ce5, (c) Ce10, and (d) Ce15; (e) Average pore size; (f) Surface porosity; (G) Sealing percentages.

determined by energy-dispersive X-ray spectroscopy (EDS). The crystal structure and phase were investigated by X-ray diffraction (XRD, Bruker, D8 Advance), and the surface chemical states were determined by X-ray photoelectron spectroscopy (XPS, Thermo Fisher, ESCALAB 250X). A focused ion beam (FIB, Scios, FEI) was used to cut and thin the samples to less than 100 nm prior to transmission electron microscopy (TEM, JEM-3200FS). A 3D laser confocal microscope (LCSM, VK-X200 series) was used to obtain the surface profile and determine the surface roughness R_a. The color bar in the LCSM image represents the difference between the highest and lowest points of the coating measured in 3D mode. Image-J was employed to analyze the pore size and distribution and calculate the sealing rate.

3. Results and discussion

Fig. 1 illustrates the discharge process in the preparation of the Ce-doped MAO coatings on the Al alloy. The discharge process exhibits three stages: surface passivation (0–60 s), passivation layer breakdown (60–300 s), and rapid and stable growth (300–600 s). During the initial 0–60 s, the Al alloy forms a dense Al_2O_3 passivation layer by oxidation in the electrolyte containing phosphate, leading to a rapid increase in the voltage. With increasing Ce concentrations, the rate of voltage increase accelerates because a larger Ce concentration diminishes the free path for ion movement in the solution, consequently reducing the conductivity of the phosphate electrolyte and resulting in a higher passivation voltage. As the voltage approaches the breakdown voltage of the passivation layer, significant charges accumulate on the surface and begin to discharge, resembling the discharge phase of a capacitor and transitioning to the arc discharge stage (60–300 s). The voltage of the sample rises progressively, with a more pronounced voltage increase observed when the Ce salt content is higher. In this stage, as the voltage goes up, the insulating passivation layer on the surface is formed gradually while the arc that punctures the passivation layer shapes the discharge pathway. Consequently, the aluminum matrix melts and disperses, and chemical or plasma reactions occur with the electrolyte to produce aluminum oxide and aluminum metal salts. The high temperature in the discharge channel facilitates the interaction between Ce^{3+} and PO_4^{3-} in the electrolyte, culminating in the formation of cerium phosphate. After 300 seconds, the process enters the rapid growth stage characterized by a gradual increase in the coating discharge voltage and intensification of the arc discharge. The resistance of the coating goes up with Ce concentration, leading to a more substantial rise in the voltage. In the subsequent to 600 s, local breakdown arcs may emerge, resulting in coating erosion. The MAO discharge process is then terminated to form the MAO coating.

Fig. 2(a–d) display the surface microstructure of the MAO coatings doped with different concentrations of Ce salts. The SEM images reveal a porous structure. The edges of the pores are like volcanic craters because the MAO discharge resembles volcanic eruption. As a result, the molten materials formed accumulate at the top of the pores. The MAO coatings doped with different amounts of Ce have different pore sizes and distributions. The undoped MAO coating has a dense pore distribution with small pore size, large pores exceeding 5 μm, and nanopores in close proximity. This is because of the lower voltage and discharging through small arcs. In contrast, the Ce-doped MAO coatings have fewer and larger pores, and the pore size increases with Ce concentrations. This is because cerium salts alter the physical properties of the electrolyte, leading to a significant voltage increase, and the metal salts and oxide impact breakdown and discharge formation. Consequently, more complex phases and higher voltages lead to preferential breakdown at weak areas forming discharge channels.

There is a significant amount of filler inside the pores of the coating doped with Ce, and internal sealing is almost accomplished. The filling materials become more prominent as the size of the pores increases,

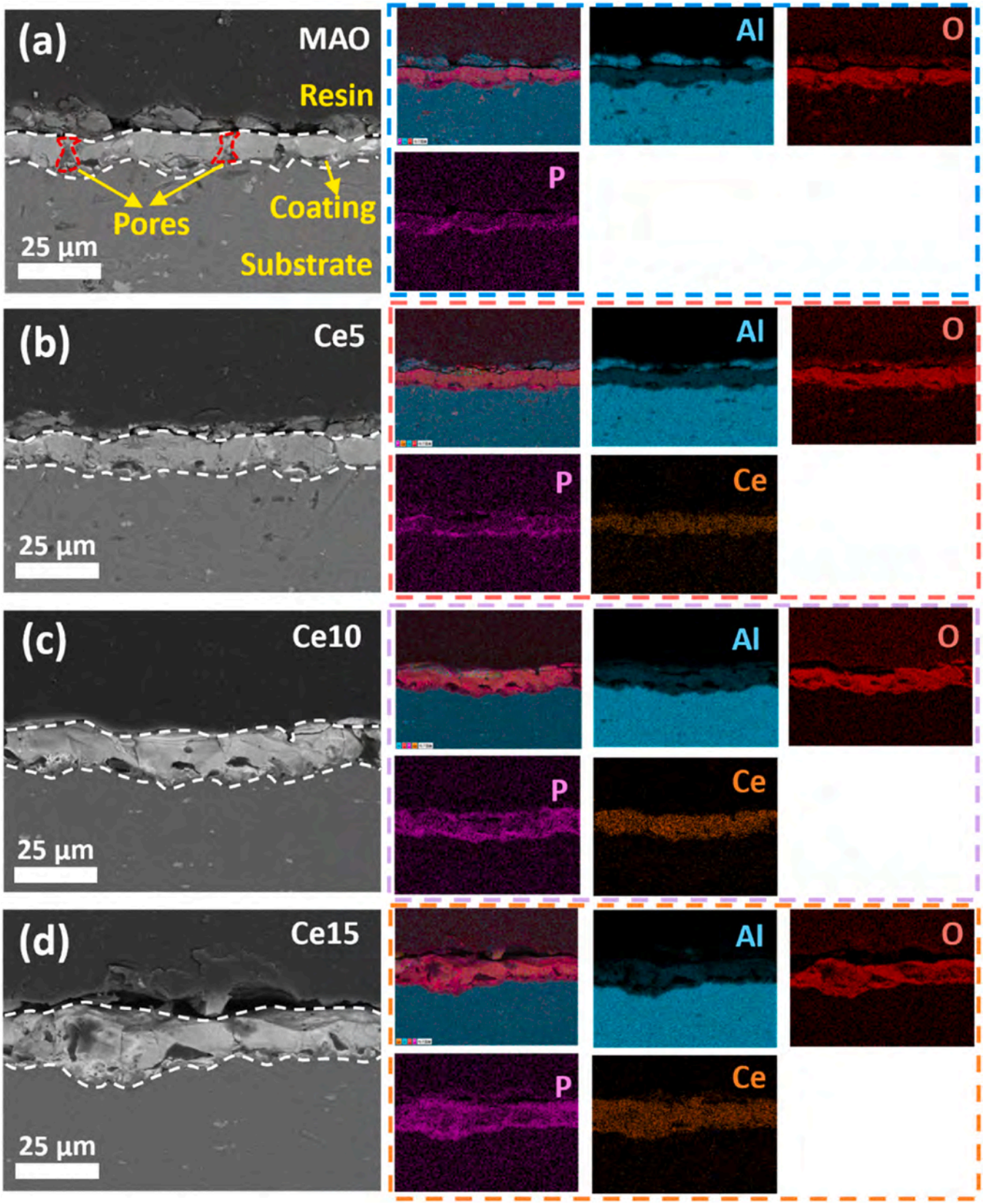

Fig. 5. Cross-sectional SEM images and EDS elemental maps (a) MAO, (b) Ce5, (c) Ce10, and (d) Ce15.

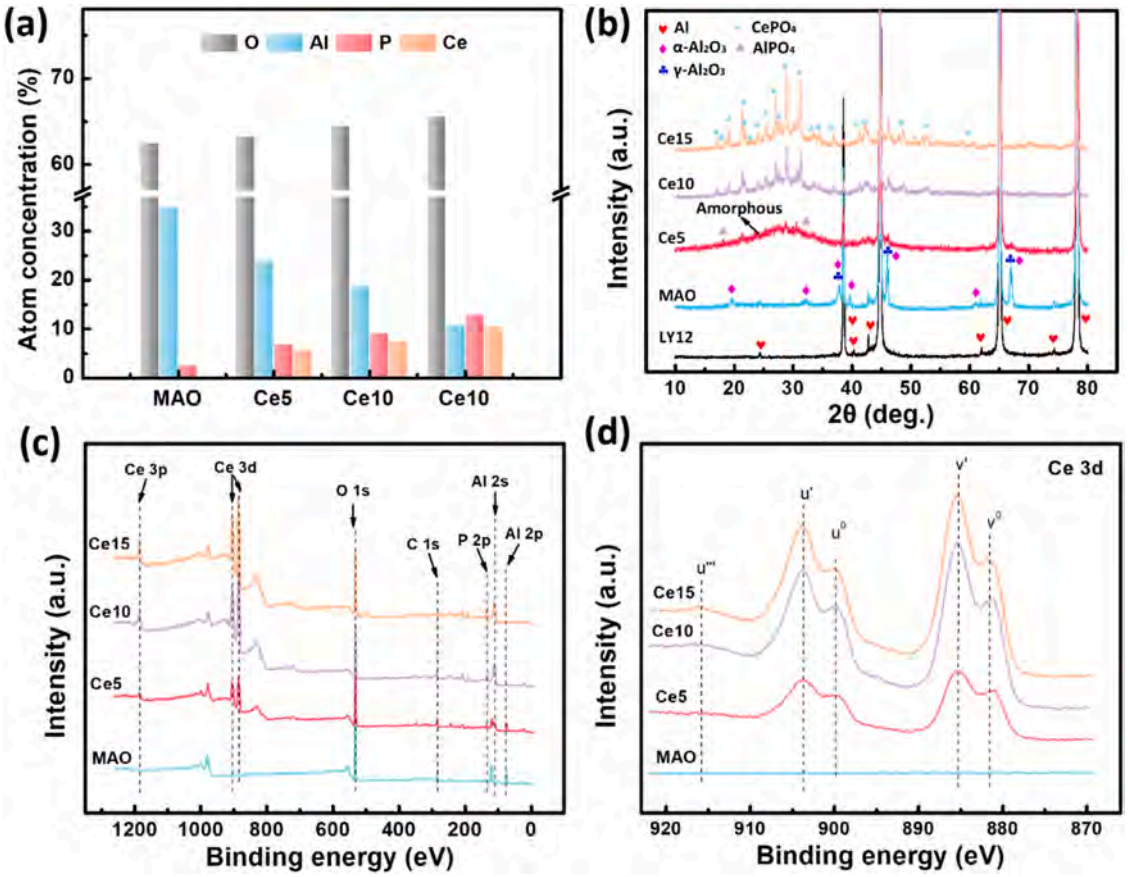

Fig. 6. Phase constituents and chemical composition of the MAO coatings doped with different concentrations of Ce salts: (a) Surface elemental concentrations by EDS, (b) XRD patterns, (c) Total spectra, and (d) Ce XPS 3*d* spectra.

which is different from many reports on added or self-generated CeO_2 nanoparticles [27,38,39]. Generally, the sealing of pores with added or self-generated nanoparticles only results in the accumulation of particles in the surface pores, leaving pores between the particles. However, the low discharge energy on the surface makes it difficult to achieve complete sealing of the pores through the melting polymerization of nanoparticles. Therefore, the corrosion resistance in long-term service environments may be compromised. This MAO coating is unique as the self-sealing of pores is accomplished in a single step. This is primarily attributed to the exogenous phosphate of Ce produced during the discharge process and backfilling of the coating, thus creating a mixture with the generated oxide and sealing the pores. The LCSM images disclose uneven molten material protrusions on the surface, but the roughness of the MAO coatings doped with different concentrations of Ce shows no significant difference (Fig. 2(a4–d4)).

Fig. 3 and Figs. S1–S2 show the EDS results of the MAO coatings revealing the presence of Al, O, and P (Fig. 3(a)) and Ce in the Ce-doped coatings. Fig. 3(b) clearly demonstrates the presence of Ce, P, and O in the pores, indicating that the molten materials seal the pores. The protrusions on the outer wall of the pores exhibit significant enrichment of Al and O due to Al_2O_3. After coating breakdown, the molten Al_2O_3 accumulates at the edges to form the outer wall of the pores. Subsequently, the phosphate of Ce and Al_2O_3 migrate back to the pores to accomplish self-sealing. The surfaces of the Ce5 and Ce15 exhibit similar elemental distributions (Figs. S1–S2).

Fig. 4 shows the porosity, size, and self-sealing percentages. Fig. 4 (a1–d1) are processed to generate the images of the pores, as illustrated in Fig. 4(a2–d2). Black color represents pores, while white represents coatings or fillers. There are numerous small pores, and the number of pores decreases after Ce doping. Many irregular black circular pores now appear white, suggesting self-sealing. Fig. 4(a2–d2) show the porosity, average pore size, and self-sealing percentages. As the Ce concentrations increase, the average pore size increases gradually, while the surface porosity decreases. The average pore sizes of MAO, Ce5, Ce10, and Ce15 are 3.14 ± 1.23 μm, 4.19 ± 1.31 μm, 4.53 ± 1.24 μm, and 5.52 ± 1.69 μm, respectively (Fig. 4(e)), while the surface porosities are 4.03 ± 0.35 %, 1.75 ± 0.27 %, 1.23 ± 0.19 %, and 0.88 ± 0.31 %, respectively (Fig. 4(f)). This is due to the increase in the discharge voltage for a larger Ce concentration, resulting in a larger density but decreased quantity. Fig. 4(g) indicates that the self-sealed pores fail when the pore size is less than 3 μm maybe because of the lower arc energy and shorter duration, as the exogenous phosphate of Ce does not melt in time to backfill the pores. When the pore size is between 3 and 10 μm, the self-sealing percentages of Ce5, Ce10, and Ce15 are 32 %, 53 %, and 42 %, respectively. The difference may be related to the nonuniformity of randomly generated arcs. Generally, the higher the sealing rate, the better the corrosion resistance. When the pore size is greater than 10 μm, the self-sealing percentages of Ce5, Ce10, and Ce15 coatings reach 100 %, suggesting that large pores can self-seal. This can be attributed to the extended duration of the large arc, which ensures the generation of phosphate of Ce and facilitates mixing with Al_2O_3 to seal the pores. Typically, larger pores are susceptible to corrosion, and the self-sealing of larger pores greatly improves the compactness of the MAO coatings.

Fig. 5 presents the cross-sectional morphology and elemental distributions of the MAO coatings doped with different concentrations of Ce. The coating thickness increases with Ce salt doping. The thicknesses of MAO, Ce5, Ce10, and Ce15 are 18.5 ± 2.5 μm, 20.2 ± 1.2 μm, 21.1 ± 1.1 μm, and 23.8 ± 2.3 μm, respectively. This is because the discharge voltage promotes the growth of the insulating layer. Typically, there is no definitive correlation between the thickness of MAO coatings and

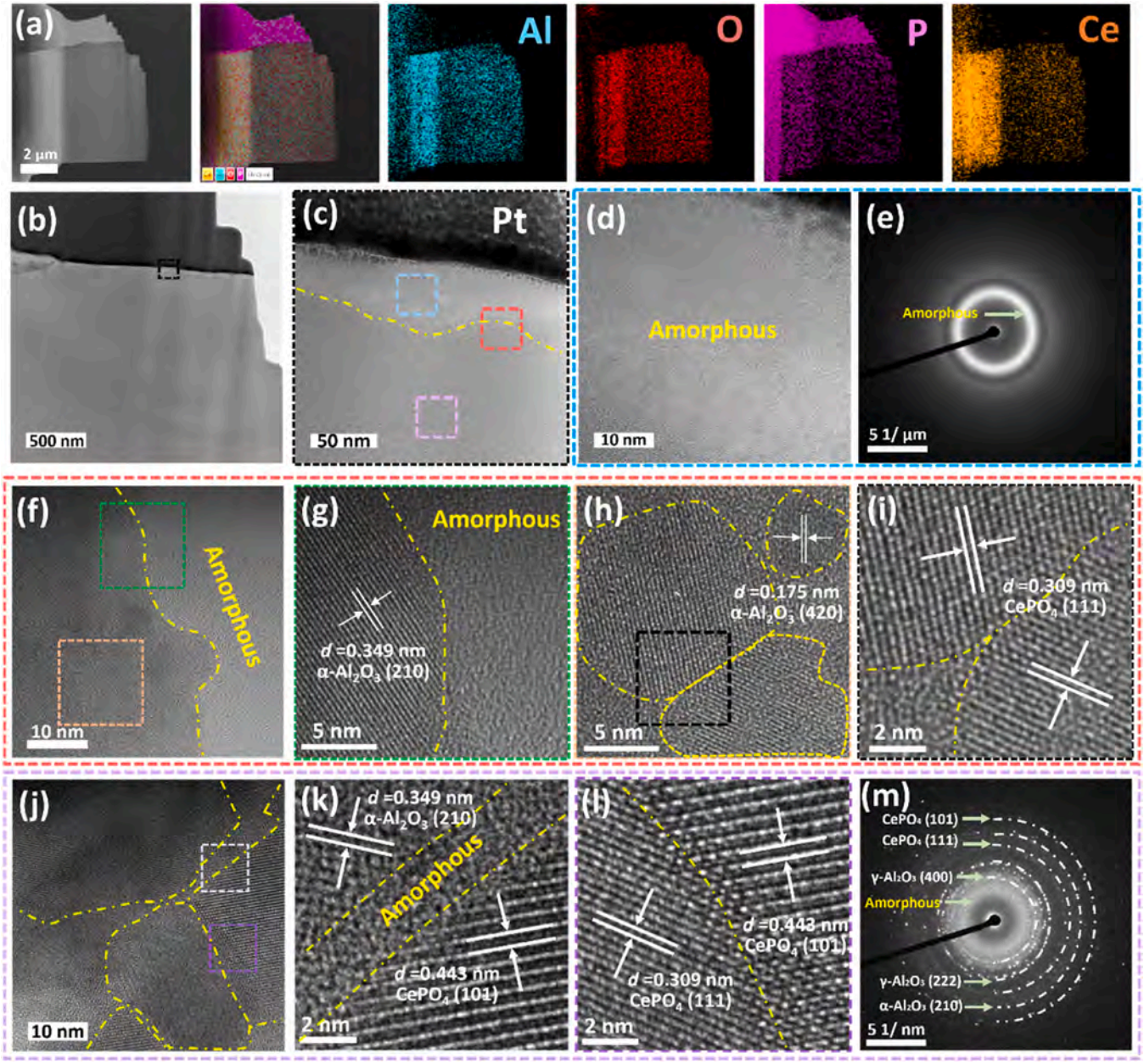

Fig. 7. TEM images of the cross-section of fillers in the pores of Ce10: (a) EDS elemental maps; (b, c) Low-magnification TEM image, (d) High-resolution TEM image and (e) SAED pattern of the blue box in (c); (f-i) High-resolution TEM image of the red box in (c), (j-l) HR-TEM image and (m) SAED pattern of the purple box in (c).

their corrosion resistance. This is because larger coating thicknesses typically lead to the formation of larger pores on the surface due to higher voltages, which ultimately does not improve corrosion resistance. There are larger pores in the MAO coating resulting from the typical discharge channel formation. In contrast, the cross-sections of Ce5, Ce10, and Ce15 do not show open pores but only a few closed pores on account of backfilling. In addition, no larger pores are observed on the surface, indicating a self-sealing effect of the molten filler. EDS shows Al, O, P, and Ce with relatively uniform distributions and no segregation.

Fig. 6(a) shows the surface elemental contents. The Al concentrations in MAO, Ce5, Ce10, and Ce15 are 34.87 at%, 23.97 at%, 18.86 at%, and 10.96 at%, respectively. The P concentrations increase gradually, indicative of the generation of phosphide. Typically, the phosphides in MAO coatings prepared in aqueous electrolytes are mainly hydrated phosphides, but after cleaning and heating, they will dehydrate to form anhydrous phosphides. In addition, the MAO contains 2.57 at% P, in comparison with 2.57 at% of Ce5 and 10.51 at% of Ce15. Fig. 6(b) shows the XRD patterns of the MAO coatings. Compared with the LY12 Al alloy, the MAO coatings exhibit α-Al_2O_3 and γ-Al_2O_3 peaks between 15 ° - 80 °, in addition to the characteristic peak of Al. Ce5, Ce10, and Ce15 show broad peaks between 15° and 35°, indicating amorphous phases in the coatings. This may be related to the faster growth rate. Ce5 shows the $CePO_4$ peak and $AlPO_4$ peaks are observed, indicating that Al not only exists as oxide. Ce10 and Ce15 show higher intensity and more crystal planes in the $CePO_4$ peak due to the larger Ce concentration. However, the $AlPO_4$ peak disappears from Ce10 and Ce15 related to the competition between high concentrations of Ce and Al for PO_4^{3-}. The results reveal that the Ce-doped coatings have mixed phases of $CePO_4$ and Al_2O_3 and also a combination of amorphous and crystalline structures.

Fig. 6(c and d) show the XPS results, which are consistent with EDS and XRD. Fig. 6(d) shows that the Ce 3*d* peak is composed of Ce $3d_{3/2}$ and $3d_{5/2}$, denoted as v^0, v', and u^0, u', respectively [40]. Additionally, for high-content Ce-doped Ce10 and Ce15 coatings, there is a

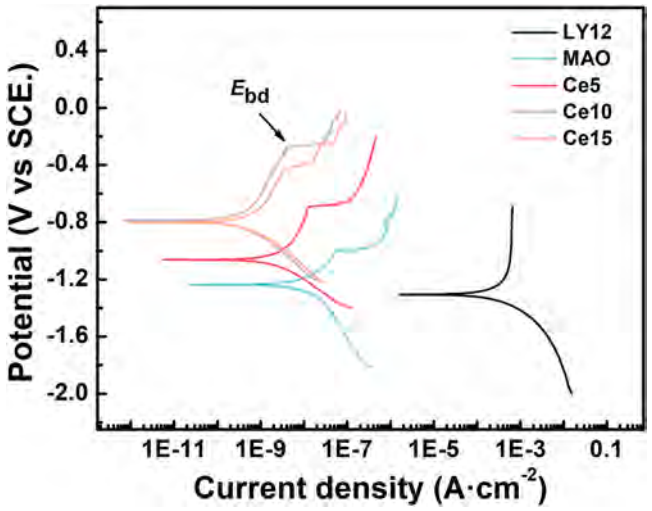

Fig. 8. Tafel results of the MAO coatings doped with different concentrations of Ce salts.

Table 1
E_{corr} and i_{corr} of the MAO coatings doped with different concentrations of Ce.

Sample	E_{corr} (V)	i_{corr} (A·cm^{-2})
LY12	−1.322	2.649×10^{-6}
MAO	−1.238	9.546×10^{-9}
Ce5	−1.063	2.381×10^{-9}
Ce10	−0.788	2.694×10^{-10}
Ce15	−0.802	3.415×10^{-10}

low-intensity peak u′′ corresponding to Ce $3d_{3/2}$ at 916.8 eV, indicating the presence of Ce^{4+}, which may correspond to CeO_2 [27]. This result indicates that Ce^{3+} in the electrolyte is mainly to react with PO_4^{3-} to form phosphides in the discharge state. However, a small amount of Ce^{3+} will oxidize and produce high valence phases at higher voltages.

To further investigate the phase composition and distribution of the self-sealing fillers, Ce10 is examined by TEM analysis, as shown in Fig. 7. The cross-section of the self-sealing fillers inside the pores is thinned by FIB to a thickness of 100 nm. EDS shows that the distributions of Al, O, P, and Ce are relatively uniform, consistent with the cross-sectional SEM image (Fig. 7(a)). As shown in Fig. 7(b), the near-surface position of the cross-section is magnified. The magnified TEM image in Fig. 7(c) shows a distinct layered structure, with the outer layer that is approximately 50 nm thick being an amorphous layer (Fig. 7(d, e)), followed by a transition layer and a mixed crystal layer on the bottom. The outer amorphous structure is related to the contact with the liquid electrolyte, which promotes rapid cooling. XPS and EDS show a mixed phase of $CePO_4$ and Al_2O_3. Amorphous phases are usually more corrosion-resistant than crystalline phases due to the absence of microscopic defects such as grain boundaries [41,42]. Fig. 7(f) shows the interface of the amorphous structure, which is mainly composed of the α-Al_2O_3 (210) crystalline phase, together with $CePO_4$ (111) grains and Al_2O_3 (420) with a size of approximately 10 nm enveloped by the amorphous phase (Fig. 7(h and i)). This may be because the lower temperature near the surface causes $CePO_4$ to form low-energy (111) crystal planes rather than high-energy crystal planes or oxides [43]. Fig. 7(j) depicts the enlarged area of the bottom purple box in Fig. 7(c). More and larger crystal phases are encapsulated in the amorphous phase, including α-Al_2O_3 on the (210) and (210) crystal planes, as well as CePO4 on the (111) and (101) crystal planes (Fig. 7(k and l). These larger grain sizes arise from the relatively high energy inside the melt, which promotes grain growth and the transition from the amorphous to crystalline state. Therefore, these grains exhibit a fuzzy interface with an amorphous/crystalline hierarchical structure. The selected-area electron diffraction (SAED) pattern confirms the mixed phase revealing the γ-Al_2O_3 phase on the (400) and (222) crystal planes. The results indicate that the molten materials inside the pores are a mixture of Al_2O_3 and $CePO_4$, primarily consisting of a blend of amorphous and nanocrystalline crystals. Furthermore, the nano amorphous layer on the surface is expected to improve the corrosion resistance of the weak pores.

Electrochemical tests are conducted on the LY12 Al alloy, MAO, Ce5, Ce10, and Ce15 in a 3.5 wt% NaCl solution to determine the corrosion resistance. The Tafel results are shown in Fig. 8 and Table 1. After MAO, the corrosion potential of LY12 Al alloy coating increases from −1.322 V to −1.238 V. Doping with Ce increases the corrosion potential. The corrosion potentials of Ce5, Ce10, and Ce15 are −1.063 V, −0.788 V, and −0.802 V, respectively. Correspondingly, the corrosion current densities decrease from 2.649×10^{-6} A·cm^{-2} of the substrate to 9.546×10^{-9} A·cm^{-2}, 2.381×10^{-9} A·cm^{-2}, 2.694×10^{-10}A·cm^{-2}, and 3.415×10^{-10} A·cm^{-2} of MAO, Ce5, Ce10, and Ce15, respectively, showing a maximum decrease of nearly four orders of magnitude. With Ce doping, the breakdown potential (E_{bd}) and corrosion resistance increase gradually, with Ce10 showing the best results, indicating that the self-sealing molten filler at weak pores hinders the penetration of the salt solution.

EIS is performed to analyze the corrosion resistance of the MAO coatings (Fig. 9). According to the Nyquist data, the MAO coatings exhibit a capacitance behavior during the initial immersing corrosion process (1 h). With increasing Ce contents, the capacitance circuit diameter increases (Fig. 9(a1)), indicating a gradual improvement in corrosion resistance. The Bode impedance plot at low frequencies corresponds to the impedance modulus [44,45]. With increasing Ce contents, the low-frequency resistance of the MAO coating increases. It increases from 3.116×10^5 Ω·cm^2 of MAO to 2.672×10^6 Ω·cm^2 of Ce5, 1.579×10^8 Ω·cm^2 of Ce10, and 1.317×10^8 Ω·cm^2 of Ce15, respectively (Fig. 9(a3)).

The impedance of the MAO coatings immersed in the salt solution for longer time durations (48 h, 168 h, and 336 h) is determined. With the exception of MAO, which exhibits inductance representing pitting corrosion after immersion for 168 and 336 h, the other coatings show a significant capacitance behavior (Fig. 9(b1–d1)). The low-frequency impedance values are utilized to assess changes in corrosion resistance. As the immersing time increases, the capacitance arc radius and low-frequency impedance decrease, indicating different degrees of corrosion (Fig. 9(b3–d3)). The capacitance arc radius and low-frequency impedance exhibit a significant decrease, possibly due to the diffusion of corrosive media and the progression of corrosion. In contrast, the low-frequency impedance of Ce5 shows a slight decrease after immersion for 48 hours due to the self-sealing effect. As the Ce concentration increases, the *in situ* growth and self-sealing effect of $CePO_4$ allay corrosion. After immersion for 336 h, the low-frequency impedance of Ce10 and Ce15 decreases slightly. Notably, the sealing rate of Ce15 in pores of 3–10 μm is lower than that of Ce10, ultimately resulting in better corrosion resistance of Ce10 compared to Ce15 [44].

The equivalent circuits (ECs) (Fig. 10) based on the time constant in the Bode phase angle plot are shown in Fig. 9(a2–d2), together with the fitted EIS results. The relaxation process at low frequencies corresponds to natural Al_2O_3 passivation, while the capacitance circuit in the mid-high frequency is related to the MAO coating. The electrochemical behavior in the low-frequency is caused by the interface reaction between the coating and Al alloy in the salt solution. Owing to the roughness, porosity, and uneven surface chemical composition of the coating, the non-uniformity of the system cannot be analyzed using ideal capacitors and resistors. Therefore, the constant phase element (CPE) expressed by Formula (1) is chosen to illustrate the non-ideal resistance and capacitance behavior of the coating [46]:

$$Z_{CPE} = \frac{1}{T(j\omega)^n} \quad -1 \le n \le 1 \tag{1}$$

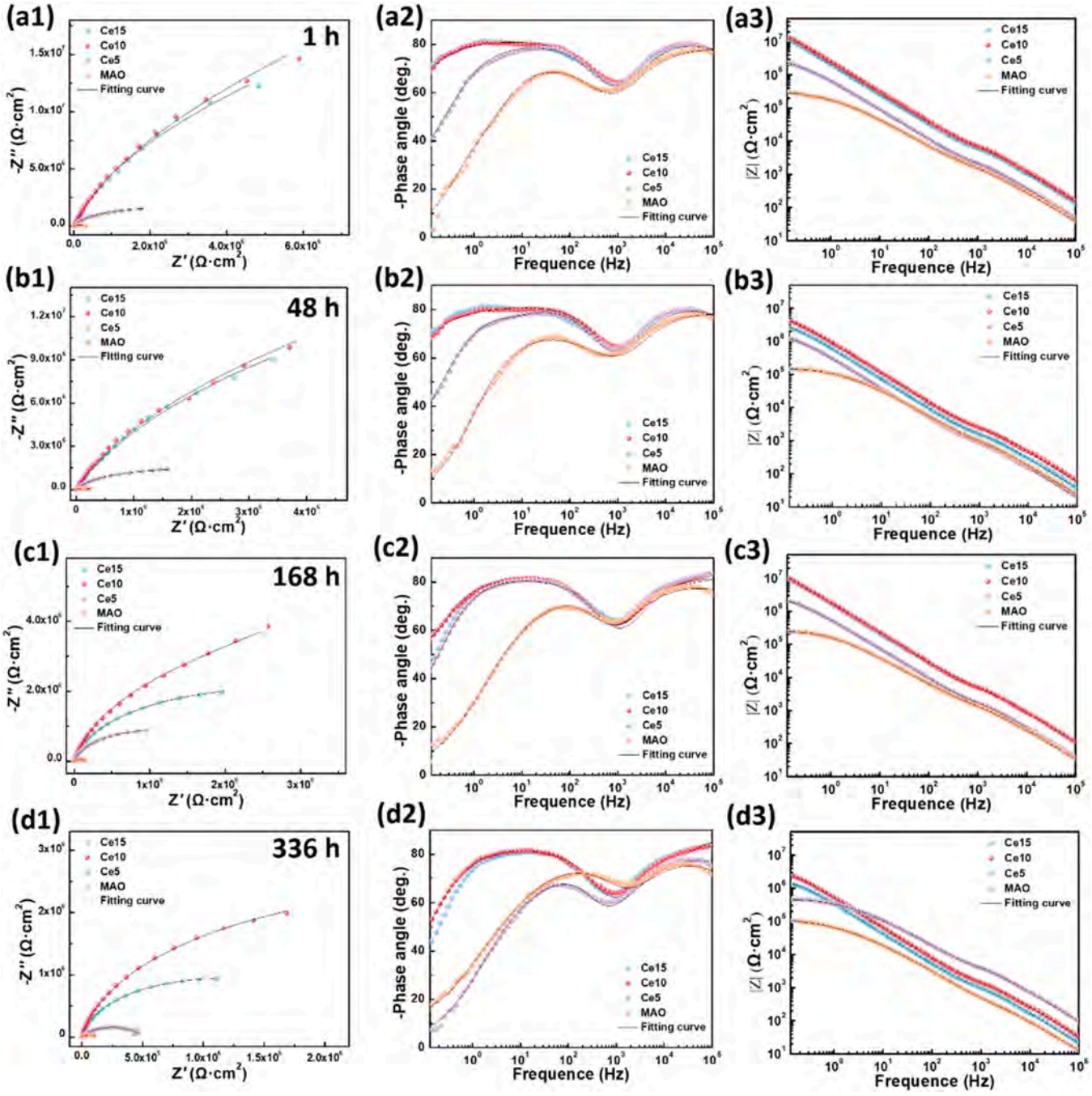

Fig. 9. EIS results of the MAO coatings doped with different concentrations of Ce after immersion in the salt solution for (a) 1 h, (b) 48 h, (c) 168 h, and (d) 336 h.

where Z_{CPE} represents the resistance of CPE, n is the CPE index, T is the CPE coefficient, ω represents the angular frequency (related to the frequency f, $\omega=2\ \pi\ f$), and $j = <$maceqn$>$ \sqrt {{\minus}1} $<$ /maceqn$>$ is the imaginary unit. When n is equal to 1, −1, and 0, respectively, it represents an ideal capacitor, an ideal inductor, and an ideal resistor. The EIS data after immersion for 1 h and 48 h are fitted by the ECs in Fig. 10(a), while the EIS data after immersion for 168 and 336 h are fitted by adding inductance (Fig. 10(b)). The EIS data of Ce5, Ce10, and Ce15 are fitted by ECs with added Warburg resistance in Fig. 10(c), where, CPE_p, and R_p are the capacitance and resistance of the external MAO coating, CPE_d and R_d are the capacitance and resistance of the interface dense layer, CPE_{dl} and R_{ct} are the double-layer capacitance and charge transfer resistance in the Faraday process, respectively, and W is the Warburg resistance.

Tables S1-S4 display the CPE and R of MAO, Ce5, Ce10, and Ce15. The higher the resistance, the better the corrosion resistance. The changes in the resistances, including low-frequency impedance R_{lf}, external coating R_p, interface dense layer R_d, and charge transfer resistance R_{ct}, are shown in Fig. 11. As the immersion time increases, the resistances decrease. After immersing for 336 h, the order of resistance is Ce10 > Ce15 > Ce5 > MAO, suggesting that the higher the Ce content, the greater the resistance and the better the corrosion resistance. The effective sealing of surface pores produces larger R_{lf}, R_p, R_d, and R_{ct} for Ce10 and Ce15. As the immersing time increases, R_d and R_{ct} decrease (Fig. 11(c, d)), indicating that the pores pose a significant corrosion risk. The corrosive medium can easily penetrate the dense layer and interface through the pores causing localized corrosion. In contrast, R_d and R_{ct} of Ce5, Ce10, and Ce15 decrease slowly, showing that pore sealing reduces

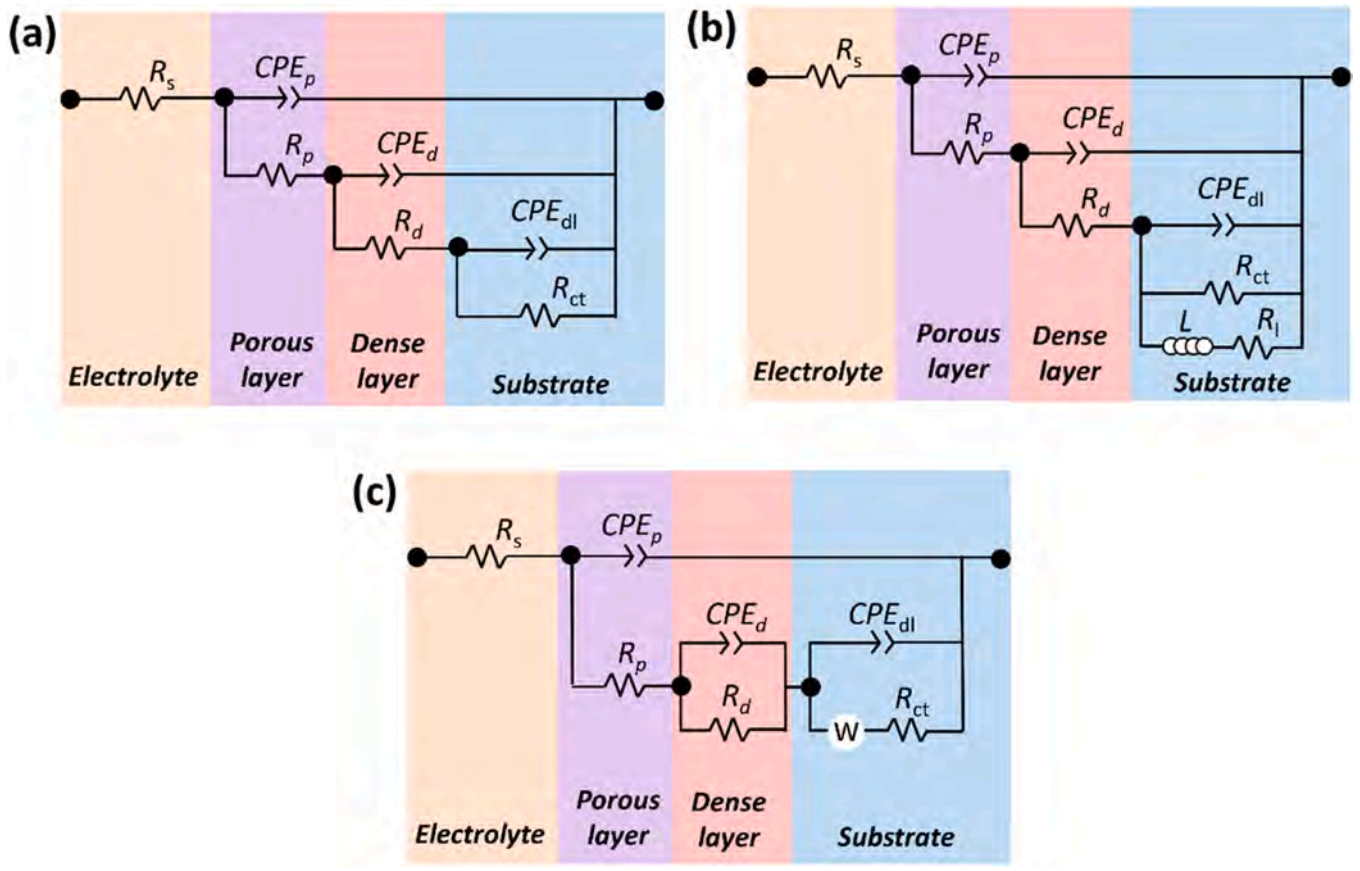

Fig. 10. ECs based on the EIS data shown in Fig. 10: (a) MAO immersed in the salt solution for 1 h and 48 h, (b) MAO immersed in the salt solution for 168 h and 336 h, and (c) Ce5, Ce10 and Ce15 immersed in the salt solution.

localized corrosion. Furthermore, during corrosion, the change in CPE is directly opposite to the resistance (Table S1-S4) because it depends on the pore area, dielectric properties, and coating thickness [47]. The newly formed corrosion products enlarge the surface area, and Cl^- increases the ion conductance of the coating, leading to a gradual increase in CPE [48]. However, it is challenging to precisely match specific CPE values as they are linked to the type and quantity of corrosion products.

Fig. 12 shows the corrosion morphology of the MAO coatings after immersion in a 3.5 wt% NaCl solution for 336 h. The surface of the undoped MAO coating is covered by dense corrosion products with a loose sponge-like structure and cracks (Fig. 12(a1–a3)) formed by Cl^- corrosion along the pores. In contrast, after immersion for 336 h, there are only some nano corrosion products on the surface and inside the pores of Ce5 (Fig. 12(b1)), while the smooth surface of the molten filler shows more interlaced corrosion products, likely formed by the release of Ce^{3+} from $CePO_4$. The changes on Ce10 and Ce15 are minimal after immersion. Only minor corrosion products are observed from the pore edges, while corrosion products are visible on the molten filling inside the pores, similar to Ce5. This indicates that cerium phosphate helps to block the corrosive medium to improve corrosion resistance. In addition, we conducted a 336 h neutral salt spray experiment on the Ce10 coating with the best corrosion resistance to evaluate its dynamic corrosion behavior. The results are shown in Fig. S5. Optical images show that no pitting corrosion was observed on the surface of Ce10 coating after 72 h, 168 h, and 336 h of neutral salt spray. The high and low magnification SEM images also indicate that there is no pitting corrosion occurring in the coating, and the molten material inside the pores still exists and the surface is covered with a layer of nano flocculent material, similar to the results of salt water immersion, indicating excellent dynamic corrosion resistance of the coating.

EDS and XPS are performed on the unsealed MAO and self-sealing Ce10 coatings after immersion in 3.5 wt% NaCl for 336 h to determine the composition of the corrosion products. Fig. 13(a) shows that the elemental composition of the MAO coating remains unchanged, consisting of Al, O, and P. The Al concentration increases slightly increases due to $Al(OH)_3$ corrosion products. The Al-O-H peak [49] in the XPS O 1 *s* spectrum indicates that the primary corrosion product of the unsealed MAO coating is $Al(OH)_3$, while the lattice O peak [50] reveals the presence of oxide (Fig. 13(b)). There is no significant change in the elemental composition of the self-sealing Ce10 coating, with Ce enriched in the pores (Fig. 13(c)). The P-O-Ce peak in the O 1 *s* spectrum [51] confirms the presence of $CePO_4$ and the Al-O-H and Ce-O-H peaks [52] show $Al(OH)_3$ and $Ce(OH)_3$ in the mixed corrosion product (Fig. 13(d)). EDS performed on Ce5 and Ce10 after corrosion exhibits the same trend (Figs. S3 and S4). The results indicate that $CePO_4$ and self-sealing mitigate long-term corrosion.

The pH and Ce^{3+} concentration changes are determined after immersion for different periods. As shown in Fig. 14(a), the pH increases with immersion time. The pH value of the solution of the unsealed MAO coating increases the fastest, reaching 7.62, 7.87, 8.15, and 8.42 after 12 h, 48 h, 168 h, and 336 h, respectively. This is due to the presence of numerous pores on the MAO coating, allowing the salt solution to easily come into contact with the substrate through the pores and undergo corrosion reactions, causing the dissolution of Al^{3+} and the release of OH^-. As the corrosion continues, although corrosion products are gradually formed and can cover local corrosion micro areas, the loose nature of these products does not block the path for ion penetration, allowing corrosion to persist. With the addition of Ce salt, the large pores on the surface of the MAO coating are sealed, making it challenging for corrosive media to penetrate the coating. Therefore, the pH of Ce5, Ce10, and Ce10 coatings increase slowly after immersion in a salt solution, reaching 8.18, 7.75, and 7.86, respectively. This indicates that self-

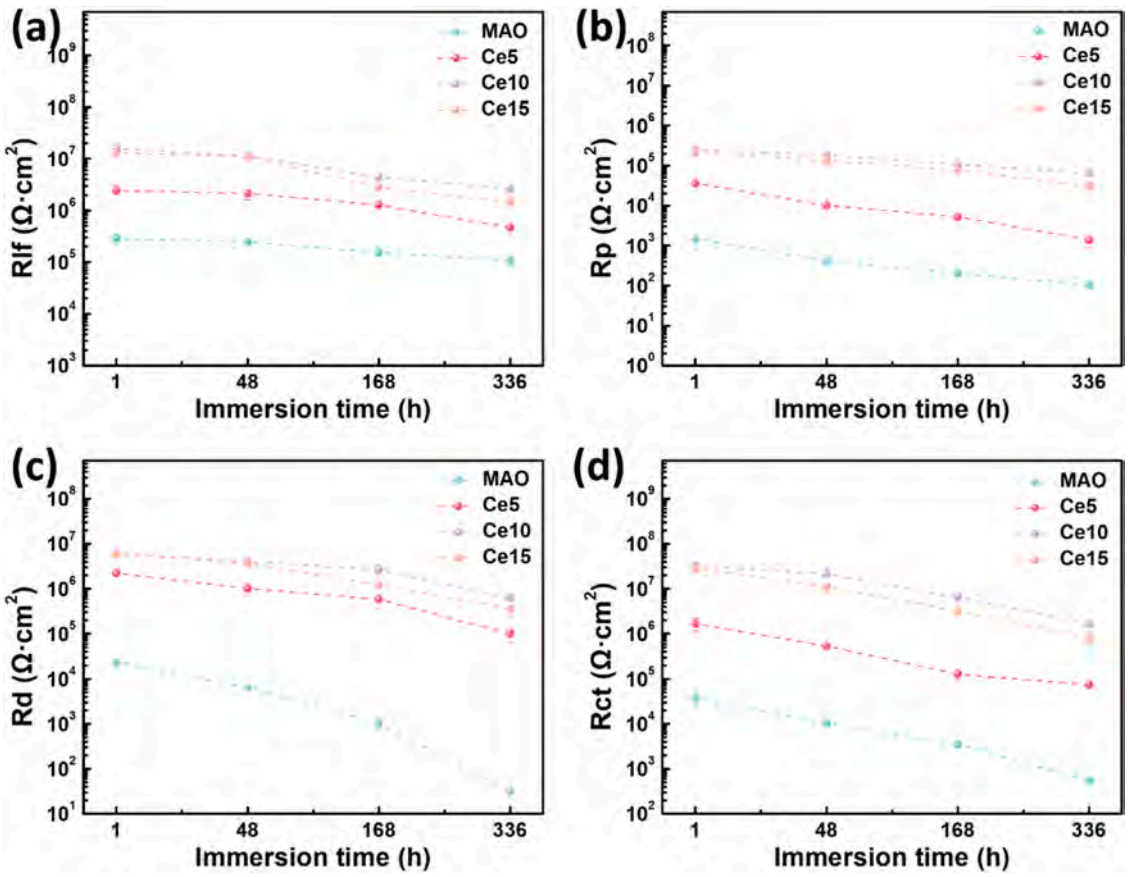

Fig. 11. Electrical parameters of the ECs of MAO coatings doped with different concentrations of Ce: (a) R_{lf}, (b) R_p, (c) R_d, and (d) R_{ct}.

sealing improves the corrosion resistance of MAO coatings. Higher Ce salt doping content leads to better corrosion resistance, effectively delaying the OH^- release at the interface.

Fig. 14(b) illustrates the changes in Ce^{3+} concentration of various samples in the salt solution after immersing. Compared with MAO coatings, Ce5, Ce10, and Ce15 coatings exhibit Ce^{3+} in the solution after immersion, with the ion concentration gradually increasing over time. After 336 h, the Ce^{3+} concentration in the solution reaches 1.65 mg/L, 1.29 mg/L, and 1.45 mg/L, respectively, indicating the release of $CePO_4$ from the coating. Moreover, the Ce5 coating shows the highest ion concentration after immersion, while the Ce10 coating has the lowest. This difference can be attributed to the excellent corrosion resistance and slower corrosion reaction of Ce10 coating compared to Ce5 coating. Therefore, the opportunity for $CePO_4$ to release Ce^{3+} is reduced. Nonetheless, this does not compromise the protective effect of the corrosion products generated by the highly corrosion-resistant Ce10 coating, as its inherent corrosion resistance and self-sealing properties are also excellent.

To further investigate the corrosion behavior of the coating/substrate interface, the MAO coating and Ce10 coating are artificially scratched and then immersed in a 3.5 wt% NaCl solution for 336 h to observe the corrosion of the interface. Fig. 15(a, b) show the morphology of artificial scratches on the MAO coating before immersion, with a visible scratch width of about 40 μm. The scratches show a typical plow groove morphology inside and expose the Al alloy substrate. Fig. 15(c, d) show the corrosion morphology changes around and inside the scratches of the MAO coating after immersion for 336 h. Compared to ordinary immersion corrosion (Fig. 12(a)), severe localized corrosion occurs around and inside the scratch once the coating is scratched, accompanied by a large accumulation of corrosion products. The corrosion product is micro-nano particles of $Al(OH)_3$, as confirmed by EDS surface scanning and line scanning results (Fig. 15(e, f)). The above results indicate that once the MAO coating is damaged, it cannot provide any protection for the substrate, and local corrosion can accelerate the corrosion of the substrate.

In contrast, the immersion corrosion results of the Ce10 coating surface shows minimal changes inside and around the artificially created scratches, with self-sealing pores present. No severe localized corrosion occurred, demonstrating excellent corrosion resistance (Fig. 16(a–c)). A thin layer of corrosion products and a small amount of microscale corrosion product flakes are observed on the flat metal surface inside (Fig. 16(d)). Surface scanning by EDS inside the scratch reveals the presence of P and Ce elements on the Al alloy substrate in addition to Al and O (Fig. 16(e)). Among these, the Al element is enriched at the edge of the scratch, while P, O, and Ce are locally enriched in the coating. Based on the morphology, it can be deduced that these are scattered coating fragments. Notably, the signal collection with a high content of Ce element throughout the entire scratch area indicates its uniform distribution. The EDS line scan results inside the scratch also show the same result (Fig. 16(f)). This interesting finding can be attributed to the self-healing properties of Ce^{3+}. When the coating is damaged, the Ce^{3+} released from the coating at the interface will enter the substrate interface with the solution and react with the local OH^- to form $Ce(OH)_3$. This eventually covers the local corrosion micro-area together with $Al(OH)_3$, providing corrosion protection for the substrate [53]. The above results indicate that the MAO coating doped with Ce salt displays self-healing properties and can provide effective active corrosion protection for the interface of the Al alloy substrate.

Due to the presence of numerous pores in the MAO coating surface of Al alloys, corrosive media can easily penetrate the coating along the pores and reach the interface between the coating and substrate, forming local pitting corrosion [54,55]. Surface sealing can delay the

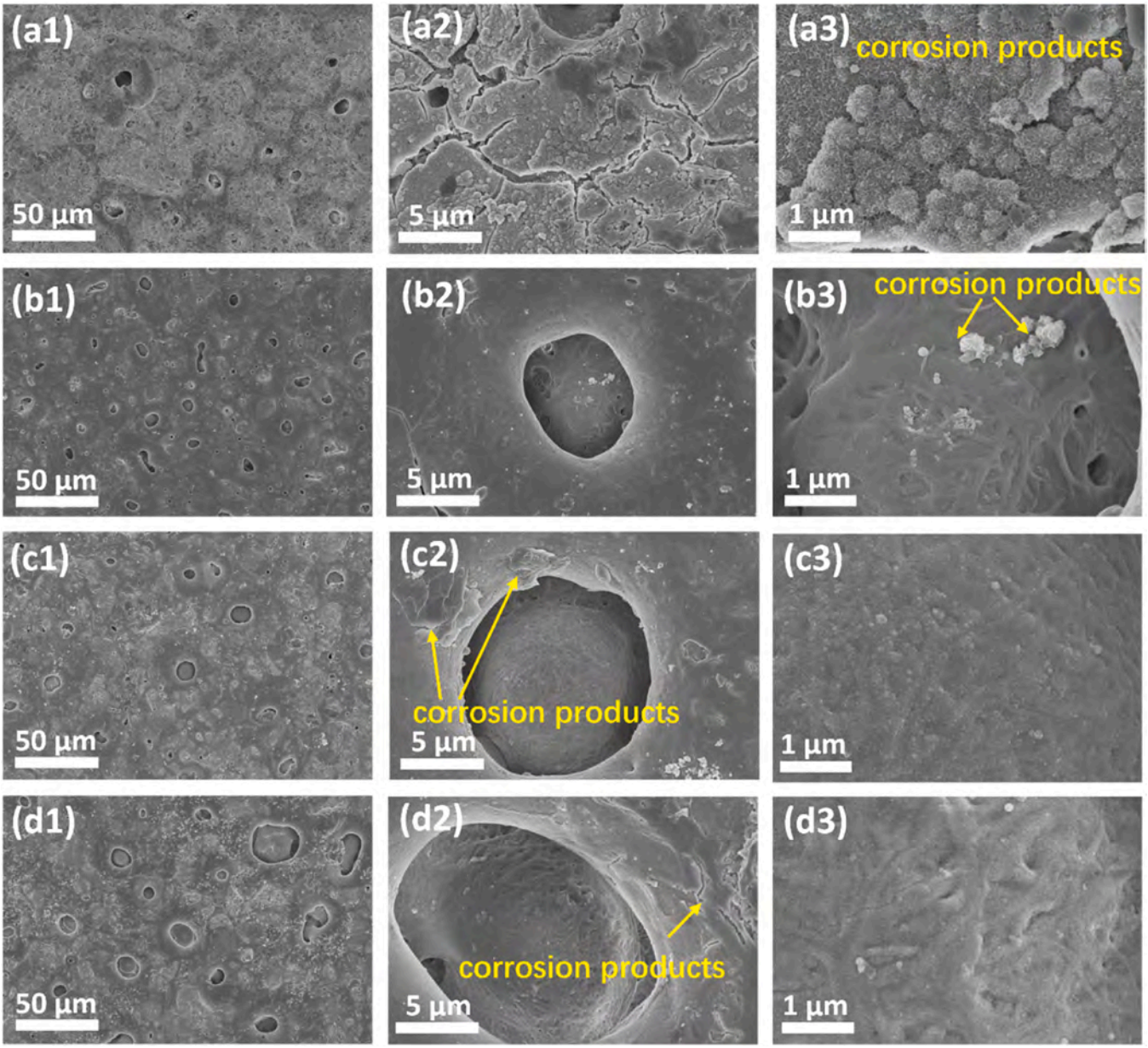

Fig. 12. SEM images of the MAO coatings doped with different concentrations of Ce salts after immersion in the salt solution for 336 h: (a) MAO, (b) Ce5, (c) Ce10, and (d) Ce15.

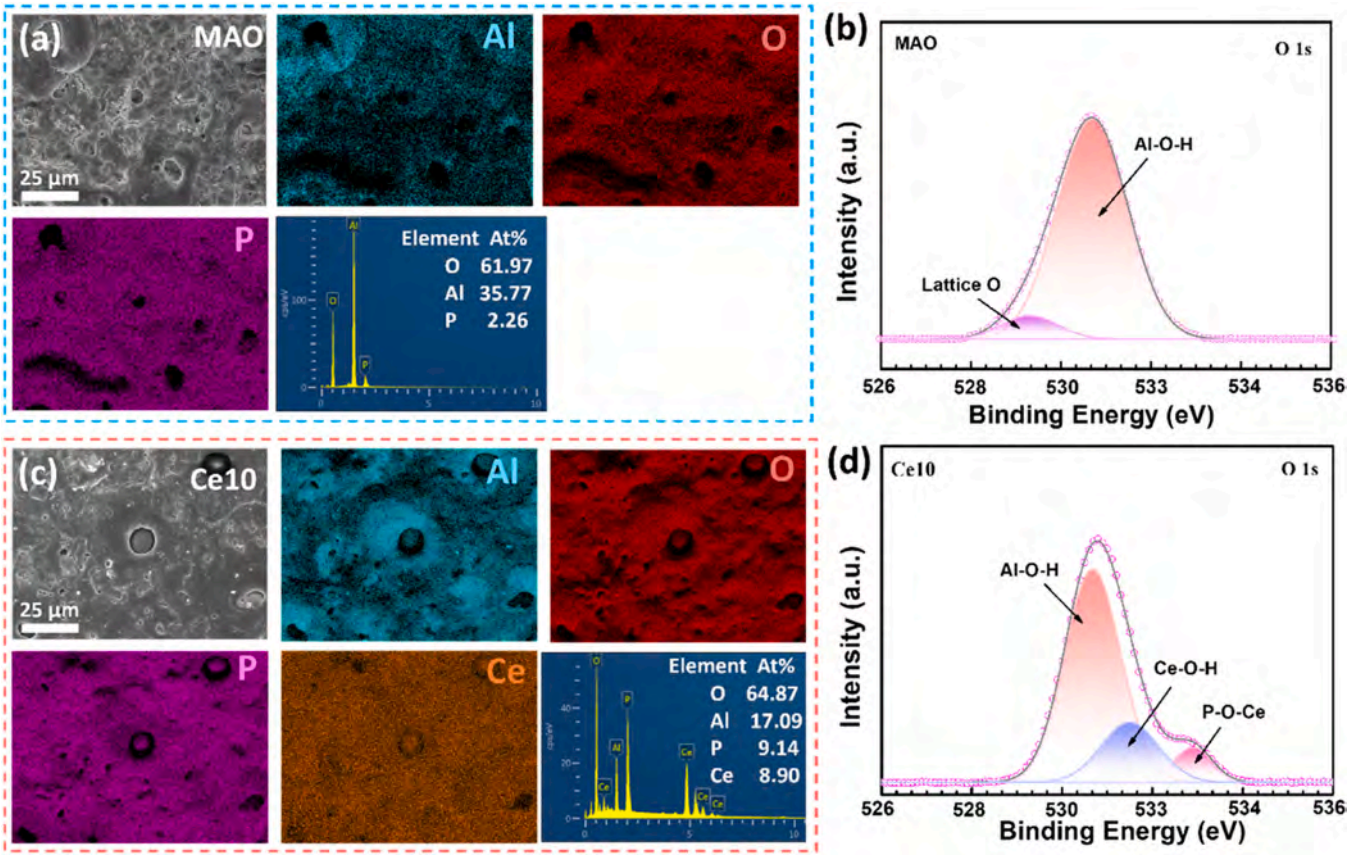

Fig. 13. (a) SEM/EDS image, elemental maps, and spectrum; (b) XPS O 1 *s* spectrum after of MAO after immersion in the salt solution for 336 h; (c) SEM/EDS image, elemental maps, and spectrum; (d) XPS O 1 *s* spectrum of Ce10 after immersion in the salt solution for 336 h.

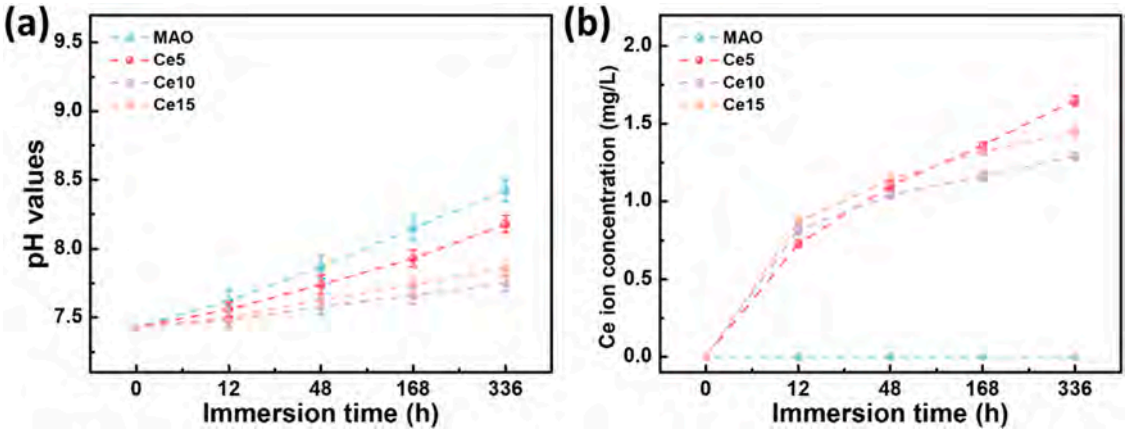

Fig. 14. (a) pH and (b) Ce^{3+} ion concentrations of the solutions after immersion in the salt solution for 336 h.

penetration of corrosive media into coatings, while endowing coatings with self-healing properties can prevent premature failure and maintain corrosion resistance [56,57]. In this work, a self-sealing and self-healing MAO coating is applied to LY12 Al alloy, resulting in a significant improvement in the corrosion resistance of the coating. Based on the above corrosion results, the corrosion resistance mechanism of MAO coating doped with $CePO_4$ on the Al alloy are further analyzed, as shown in Fig. 17.

For the MAO coating without Ce doping, Cl^- in the corrosive medium is difficult to corrode the coating body Al_2O_3, but it is easy to penetrate the coating along the internal pores to reach the substrate interface, causing anodic dissolution of the Al [58], as shown in formula (2):

$$Al \rightarrow Al^{3+} + 3e^-. \quad (2)$$

At the cathode, an oxygen absorption reaction occurs [59], as shown in formula (3):

$$O_2 + 2H_2O + 4e^- \rightarrow 4OH^-. \quad (3)$$

The Al^{3+} generated at the corrosion interface react rapidly with OH^- to generate the corrosion product $Al(OH)_3$ [60], which deposits on the corrosion micro zone. However, the corrosion product $Al(OH)_3$ is not stable and can be further eroded by Cl^- to the formation of loose Al $(OH)_{3-n}Cl_n$ (where n = 1, 2, 3) [61], as shown in formulas (4, 5):

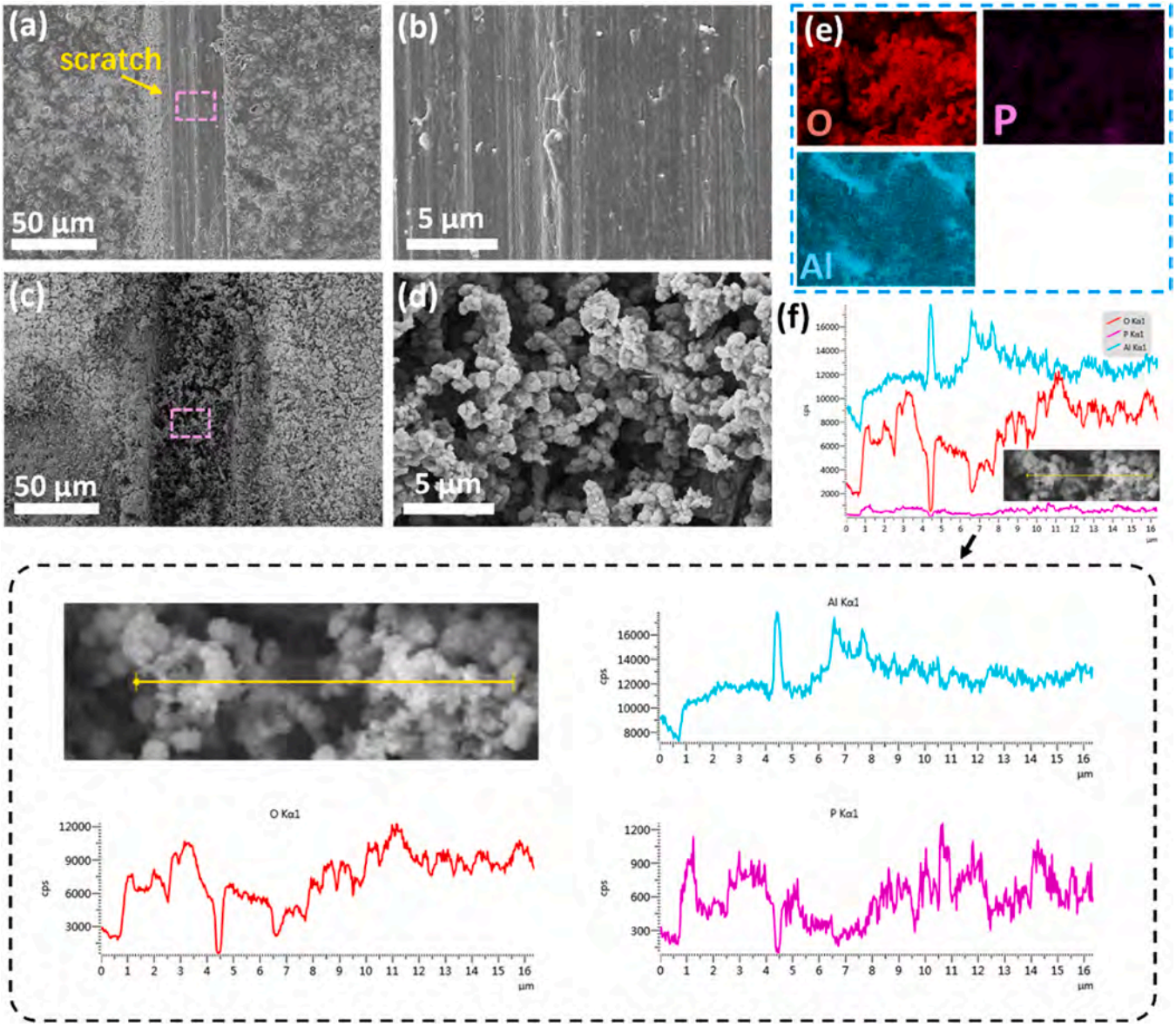

Fig. 15. SEM images of the scratched MAO coating: (a, b) Before and (c, d) After immersion in the salt solution for 336 h; (e) EDS elemental maps and (f) Line profiles of the scratches after immersion.

$$Al^{3+} + 3OH^{-} \rightarrow Al(OH)_3 \quad (4)$$

$$Al(OH)_3 + nCl^{-} \rightarrow Al(OH)_{3-n}Cl_n + nOH^{-},\ n = 1, 2, 3 \quad (5)$$

The loose corrosion products lack protective properties, which accelerates the immersion corrosion process and ultimately leads to the failure of MAO coatings due to the accelerated formation of localized pitting.

For the MAO coating doped with Ce, the in-situ grown $CePO_4$ and Al_2O_3 combine to create a mixed melt that fills the pores. This creates a self-sealing effect that effectively prevents the penetration of corrosive media along the pores. Compared to many studies on Ce-doped MAO coatings, nanoparticles are unable to completely seal, resulting in gaps between particles that serve as defects incapable of withstanding long-term corrosion. The $CePO_4$ in the coating is mainly uniformly distributed in the form of nanocrystals throughout the coating. During the long-term corrosion, it is inevitable that the corrosive medium will locally penetrate the interface of coating/substrate and undergo the reaction of formula (3−5). The generated $Al(OH)_3$ will further dissolve with Cl^- to create a corrosion micro-zone. The nearby $CePO_4$ in the coating is likely to release Ce^{3+} and generate the corrosion product $Ce(OH)_3$ with a low solubility product constant ($K_{sp} = 6.3 \times 10^{-24}$) at a faster rate, as shown in formula (6) [53,62]:

$$Ce^{3+} + 3OH^{-} \rightarrow {}^{Ce}(OH)_3 \quad (6)$$

Typically, the corrosion product of loose $Al(OH)_3$ is unable to effectively prevent further diffusion corrosion of Cl^-, resulting in the longitudinal development of localized pitting corrosion. In contrast, the simultaneous deposition of $Ce(OH)_3$ enhances the density of $Al(OH)_3$, forming a mixed corrosion product layer, effectively preventing local pitting corrosion. The coating thus exhibits self-healing properties, effectively alleviating the failure of MAO coatings caused by local corrosion and coating detachment, greatly improving the long-term corrosion protection performance of MAO coatings on Al alloy substrates.

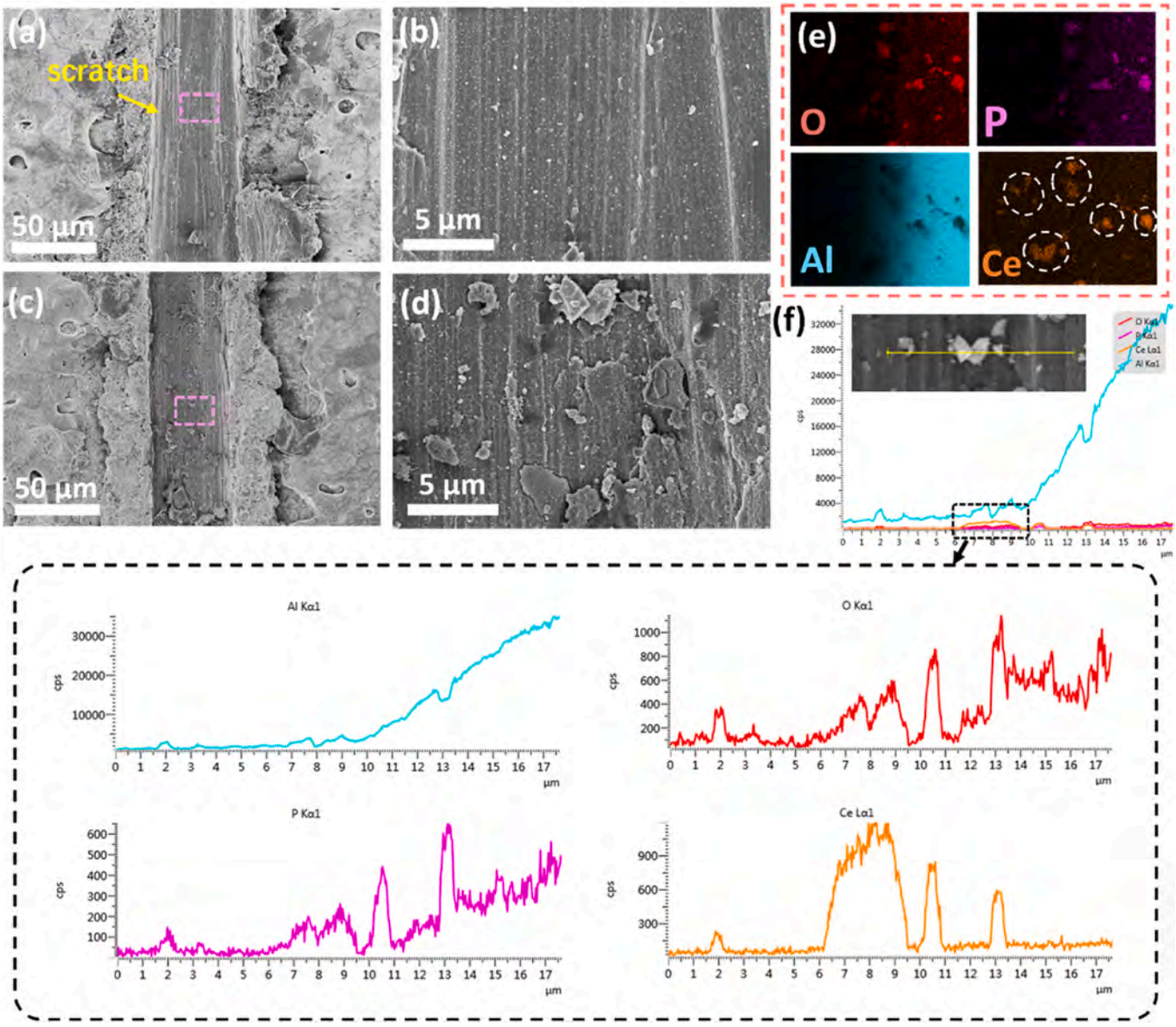

Fig. 16. SEM images of the scratched Ce10 coating: (a, b) Before and (c, d) After immersion in the salt solution for 336 h; (e) EDS elemental maps and (f) Line scans of the scratched Ce10 coating after immersion.

4. Conclusion

Self-sealing and self-healing MAO coatings are prepared on the LY12 Al alloy by a one-step method. Ce reacts with the phosphate electrolyte during the discharge process to form $CePO_4$, which is mixed with molten Al_2O_3 to fill the pores and create self-sealing effects. The mixed melt consists of an amorphous layer approximately 50 nm thick, which offers better corrosion protection than the crystalline phase. The $CePO_4$ nanocrystals mixed with Al_2O_3 produce a mixed amorphous structure. Analysis of the surface pores indicates that pores larger than 10 μm undergo complete sealing. Electrochemical tests show that Ce-doped MAO coatings have higher corrosion potentials, smaller corrosion current densities, and excellent corrosion resistance compared to undoped MAO coating. With increasing Ce concentrations, enhanced corrosion protection is accomplished. After immersion in a salt solution for 336 h, Ce10 and Ce15 show almost no pitting corrosion due to self-sealing. The results of salt solution immersion following artificial scratching confirm the self-healing properties of the Ce-doped MAO coatings. $CePO_4$ in the coating releases Ce^{3+} during immersion and reacts with locally generated OH^- to form $Ce(OH)_3$. This fills the porous structure of the corrosion product $Al(OH)_3$ and creates a more uniform and dense corrosion product layer that prevents pitting at the coating/substrate interface. The self-sealing and self-healing MAO coating provides long-term corrosion protection for Al alloys to withstand harsh working conditions.

CRediT authorship contribution statement

Zongmin Sun: Supervision, Methodology, Investigation, Formal analysis. **Chengyu Wang:** Supervision, Methodology. **Aihui Huang:** Investigation, Formal analysis, Conceptualization. **Zishuo Ye:** Software. **Tao Ying:** Visualization, Investigation. **Liping Zhou:** Validation, Supervision, Formal analysis. **Shu Xiao:** Writing – review & editing, Methodology, Investigation, Data curation. **Paul K. Chu:** Writing – review & editing, Funding acquisition, Conceptualization. **Xiaoqin Zeng:** Writing – review & editing, Methodology, Investigation, Conceptualization. **Chao Yang:** Writing – original draft, Investigation, Funding acquisition, Data curation, Conceptualization.

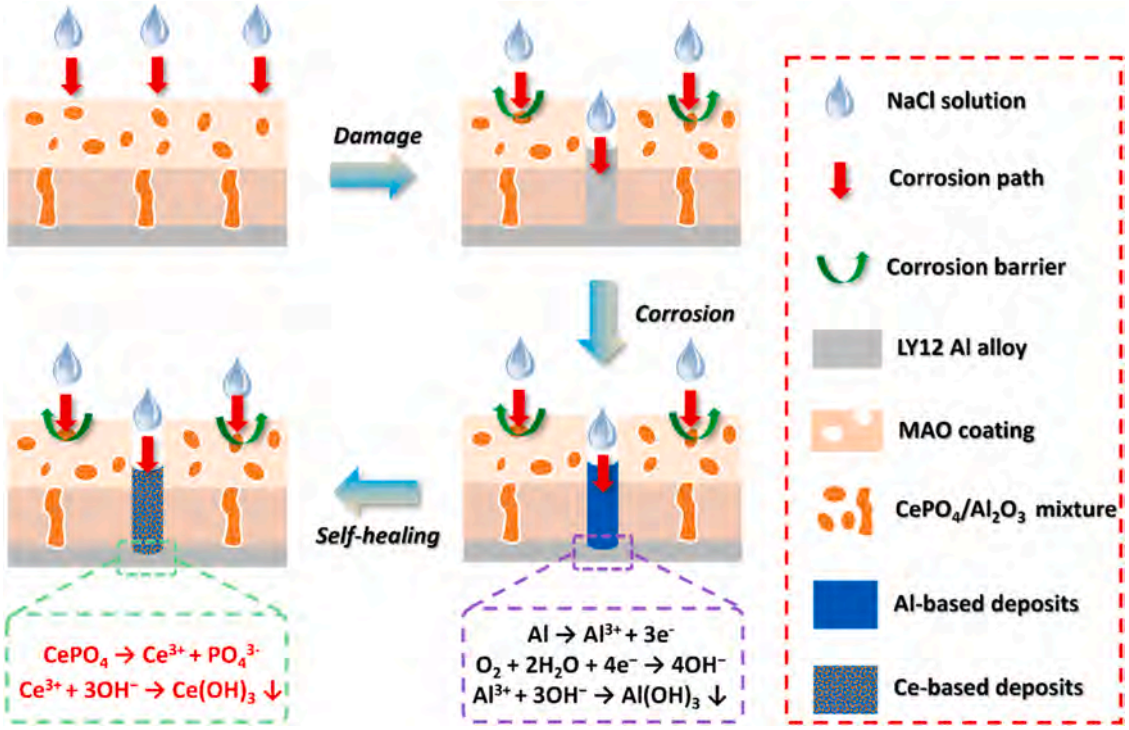

Fig. 17. Schematic illustration of the self-healing and corrosion mechanism of the Ce-doped MAO coating on the LY12 Al alloy.

Declaration of Competing Interest

The authors declare that they have no known competing financial interests or personal relationships that could have appeared to influence the work reported in this paper.

Acknowledgments

This work was financially supported by the National Natural Science Foundation of China (No. 52401101), the Postdoctoral Fellowship Program of CPSF under Grant Number GZC20231545, China Post-doctoral Science Foundation (2024T170557 and 2023M742224), Shanghai Post-doctoral Excellence Program (No. 2023440), and City University of Hong Kong Donation Research Grants (Nos. DON-RMG 9229021 and 9220061).

Appendix A. Supporting information

Supplementary data associated with this article can be found in the online version at doi:10.1016/j.corsci.2025.112706.

Data availability

Data will be made available on request.

References

[1] S. Sun, Q. Zheng, D. Li, J. Wen, Long-term atmospheric corrosion behaviour of aluminium alloys 2024 and 7075 in urban, coastal and industrial environments, Corros. Sci. 51 (2009) 719–727.
[2] P. Zhou, L.X. Yang, Y.J. Hou, G.Q. Duan, B.X. Yu, X.J. Li, Y.F. Zhai, B. Zhang, T. Zhang, F.H. Wang, Grain refinement promotes the formation of phosphate conversion coating on Mg alloy AZ91D with high corrosion resistance and low electrical contact resistance, Corros. Commun. 1 (2021) 47–57.
[3] S. Zhang, C. Wang, S.X. Zhao, A.Q. Niu, Y.L. Ma, B.C. Liu, Enhanced long-term corrosion protection of 2A14 aluminum alloy: hybrid effect of micro-arc oxidation coating and cerium based conversion treatment, Surf. Coat. Technol. 464 (2023) 129579.
[4] H.H. Xie, L. Zhang, X.Y. Zhang, Y. Han, A hierarchically structured coating on 2A12-T4 aluminum alloy for anti-wear and corrosion, Corros. Sci. 207 (2022) 110598.
[5] C. Yang, S.H. Cui, Y.C. Weng, Z.C. Wu, L.L. Liu, Z.Y. Ma, X.B. Tian, Ry.K.Y. Fu, P. K. Chu, Z.Z. Wu, Scalable superhydrophobic T-shape micro/nano structured inorganic alumina coatings, Chem. Eng. J. 409 (2021) 128142.
[6] Y. Lv, T. Hashimoto, X.R. Zhou, X.X. Zhang, Influence of thermomechanical treatment on the corrosion behaviour of 2A97 Al-Cu-Li alloy, Corros. Commun. 15 (2024) 13–23.
[7] X. Verdalet-Guardiola, B. Fori, J.P. Bonino, S. Duluard, C. Blanc, Nucleation and growth mechanisms of trivalent chromium conversion coatings on 2024-T3 aluminium alloy, Corros. Sci. 155 (2019) 109–120.
[8] M.M. Cui, D.I. Njoku, B.W. Li, L.H. Yang, Z.K. Wang, B.R. Hou, Y. Li, Corrosion protection of Aluminium Alloy 2024 through an epoxy coating embedded with smart microcapsules: the responses of smart microcapsules to corrosive entities, Corros. Commun. 1 (2021) 1–9.
[9] C. Yang, L.Y. Sheng, C.C. Zhao, D. Wu, Y.F. Zheng, Regulating the ablation of nanoparticle-doped MAO coating on Mg alloy by MgF_2 passivation layer construction, Mater. Lett. 355 (2024) 135559.
[10] V. Egorkin, S.V. Gnedenkov, S.L. Sinebryukhov, I.E. Vyaliy, A.S. Gnedenkov, R. G. Chizhikov, Increasing thickness and protective properties of PEO-coatings on aluminum alloy, Surf. Coat. Technol. 334 (2018) 29–42.
[11] Y.X. Gao, Y.N. Chen, S. Xiao, T.J. Li, H. Wu, X.Y. Meng, W.J. Li, S.Y. Fan, Z.S. Ye, G. H. Chen, P.K. Chu, Effects and mechanism of Zn on the structure and corrosion resistance of microarc oxidation coatings on aluminum alloy, Appl. Surf. Sci. 659 (2024) 159909.
[12] C. Yang, P.H. Chen, W.X. Wu, L.Y. Sheng, Y.F. Zheng, P.K. Chu, A review of corrosion-resistant PEO coating on Mg alloy, Coatings 14 (2024) 451.
[13] I. Shchedrina, A.G. Rakoch, G. Henrion, J. Martin, Non-destructive methods to control the properties of MAO coatings on the surface of 2024 aluminium alloy, Surf. Coat. Technol. 417 (2014) 27–44.
[14] C. Yang, C.Y. Wang, Z. Shen, L.P. Zhou, L.Y. Sheng, D.K. Xu, Y.F. Zheng, P.K. Chu, S. Xiao, T. Ying, X.Q. Zeng, Simultaneous Improvement of Wear and Corrosion Resistance of Microarc Oxidation Composite Coatings on ZK61 Mg Alloy by Doping With ZrO2 Nanoparticles, J. Mater. Sci. Technol. https://doi.org/10.1016/j.jmst.2024.10.023.
[15] J.H. Lee, S.J. Kim, Enhancement of wettability by wet surface modification and application of rare-earth element in sealing of ceramic oxide thin film on Al alloy, J. Nanosci. Nanotechnol. 16 (2016) 11797–11801.
[16] C.Y. Li, X.L. Fan, R.C. Zeng, L.Y. Cui, S.Q. Li, F. Zhang, Q.K. He, M.B. Kannan, H. W. Jiang, D.C. Chen, S.K. Guan, Corrosion resistance of in-situ growth of nanosized $Mg(OH)_2$ on micro-arc oxidized magnesium alloy AZ31—influence of EDTA, J. Mater. Sci. Technol. 35 (2019) 1088–1098.
[17] H. Yan, J.C. Wang, M. Cai, X. Wang, X. Wang, S.J. Sun, X.Q. Fan, L. Zhang, H. Li, W. Li, M.H. Zhu, Towards long-term corrosion and wear protection of Al alloy: synergy of Ti3C2Tx flake and micro-arc oxidation coating, Corros. Sci. 174 (2020) 108813.

[18] A. Alabbasi, A. Mehjabeen, M.B. Kannan, Q.S. Ye, C. Blawert, Biodegradable polymer for sealing porous PEO layer on pure magnesium: an in vitro degradation study, Appl. Surf. Sci. 301 (2014) 463–467.

[19] C. Yang, J. Huang, S.H. Cui, R.K.Y. Fu, L.Y. Sheng, D.K. Xu, X.B. Tian, Y.F. Zheng, P.K. Chu, Z.Z. Wu, NaF assisted preparation and the improved corrosion resistance of high content ZnO doped plasma electrolytic oxidation coating on AZ31B alloy, J. Magnes. Alloy 12 (2024) 3602–3615.

[20] D.L. Shen, H.W. Li, R.J. Yang, S.J. Zhou, W.Z. Li, The effect of post-sealing incorporation with different Na2MoO4 concentrations on the corrosion behavior of 6063 aluminum alloy coated via micro-arc oxidation coating, Mater. Today Commun. 41 (2024) 110593.

[21] Z.U. Rehman, D.J. Choi, Investigation of ZrO2 nanoparticles concentration and processing time effect on the localized PEO coatings formed on AZ91 alloy, J. Magnes. Alloy. 7 (2019) 555–565.

[22] E.H. Yang, R.X. Yang, W. Wei, Q.F. Mo, F.Y. Liang, D. Li, W.Z. Li, Corrosion resistance and antibacterial properties of hydrophobic modiffed Ce-doped micro-arc oxidation coating, J. Mater. Res. Technol. 29 (2024) 3303–3316.

[23] S.P. Ji, Y.C. Weng, Z.Z. Wu, Z.Y. Ma, X.B. Tian, R.K.Y. Fu, H. Lin, G.S. Wu, P. K. Chu, F. Pan, Excellent corrosion resistance of P and Fe modified micro-arc oxidation coating on Al alloy, J. Alloy. Compd. 710 (2017) 452–459.

[24] Q. Huang, L.L. Liu, Z.Z. Wu, S.P. Ji, H. Wu, P.H. Chen, Z.Y. Ma, Z.C. Wu, R.K.Y. Fu, H. Lin, X.B. Tian, F. Pan, P.K. Chu, Corrosion-resistant plasma electrolytic oxidation coating modified by Zinc phosphate and self-healing mechanism in the salt-spray environment, Surf. Coat. Technol. 384 (2020) 125321.

[25] D. Jiang, X.C. Xia, J. Hou, G.Y. Cai, X.X. Zhang, Z.H. Dong, A novel coating system with self-reparable slippery surface and active corrosion inhibition for reliable protection of Mg alloy, Chem. Eng. J. 373 (2019) 285–297.

[26] D. Jiang, X.C. Xia, J. Hou, X.X. Zhang, Z.H. Dong, Enhanced corrosion barrier of microarc-oxidized Mg alloy by self-healing superhydrophobic silica coating, Ind. Eng. Chem. Res. 58 (2019) 165–178.

[27] G.Y. Cai, S. Xiao, C.M. Deng, D. Jiang, X.X. Zhang, Z.H. Dong, CeO_2 grafted carbon nanotube via polydopamine wrapping to enhance corrosion barrier of polyurethane coating, Corros. Sci. 178 (2021) 109014.

[28] Y. Lv, Y.P. Zhang, X.Z. Meng, Z.H. Dong, X.X. Zhang, Construction of a PEO/Mg–Mn LDH composite coating on Mg−Ag−Mn alloy for enhanced corrosion resistance and antibacterial potential, Ceram. Int. 49 (2023) 35632–35643.

[29] Y. Wang, T.L. Wang, S.B. Liu, Z. Wei, T.C. Zhang, S.J. Yuan, Bilayer diatomite-based composite coatings with superhydrophobic and self-healing properties for enhanced anticorrosion of AZ31B magnesium alloys, Surf. Coat. Technol. 489 (2024) 131151.

[30] B. Lin, J. Wang, H. Zhang, Y. Wang, H. Zhang, J. Tang, J. Hou, H. Zhang, M. Sun, Self-healing performance of ethyl-cellulose based supramolecular gel coating highly loaded with different carbon chain length imidazoline inhibitors in NaCl corrosion medium, Corros. Sci. 197 (2022) 110084.

[31] C.Y. Wang, M.S. Sun, C. Yang, H.Y. Wang, J. Wang, L. Mao, Y. Yang, T. Ying, P.K. Chu, X.Q. Zeng, Degradation Behavior of Pure Mg in the Physiological Medium and Growth Mechanism of Surface Corrosion Product Films, J. Magnes. Alloy. https://doi.org/10.1016/j.jma.2024.05.012.

[32] P.J. Denissen, S.J. Garcia, Cerium-loaded algae exoskeletons for active corrosion protection of coated AA2024-T3, Corros. Sci. 128 (2017) 164–175.

[33] S. Zhang, Y.L. Ma, S.X. Zhao, W.H. Dai, B.C. Liu, Enhanced coating system corrosion protection of 2A14 Al alloy by modiffed cerium seal PEO pretreatment, Corros. Sci. 235 (2024) 112203.

[34] X.H. Liu, L.Q. Zhu, H.C. Liu, W.P. Li, Investigation of MAO coating growth mechanism on aluminum alloy by two-step oxidation method, Appl. Surf. Sci. 293 (2014) 12–17.

[35] Y. Tang, C.P. Yang, Q.Q. Sun, L.K. Wu, F.H. Cao, Effects of TiC particles on tribological and corrosion resistance of PEO coating on TC4 alloy, Corros. Commun. 14 (2024) 1–10.

[36] W.H. Yao, L. Wu, J.F. Wang, B. Jiang, D.F. Zhang, M. Serdechnova, T. Shulha, C. Blawert, M.L. Zheludkevich, F.S. Pan, Micro-arc oxidation of magnesium alloys: a review, J. Mater. Sci. Technol. 118 (2022) 158–180.

[37] C.Y. Jiang, Y.M. Wang, S.Q. Wang, Y.C. Zou, J.H. Ouyang, D.C. Jia, Y. Zhou, Growth characteristics and properties of plasma electrolytic oxidation coatings produced in different electrolytes on SiCp/Al composite, Mater. Charact. 205 (2023) 113344.

[38] G.F. Ma, Z.P. Li, X.R. Zhao, Z.Y. Wang, R.H. Kou, S.N. Sun, Y. Sun, S.Y. Wang, Y. L. Yang, Microstructure and corrosion-resisting properties of CeO_2-SiO_2-Al_2O_3 composite coatings prepared by plasma electrolytic oxidation on aluminum matrix composites, J. Alloy. Compd. 1008 (2024) 176673.

[39] M. Mohedano, C. Blawert, M.L. Zheludkevich, Silicate-based plasma electrolytic oxidation (PEO) coatings with incorporated CeO2 particles on AM50 magnesium alloy, Mater. Des. 86 (2015) 735–744.

[40] J. Holgado, G. Munuera, J. Espinós, A.J. González-Elipe, XPS study of oxidation processes of CeOx defective layers, Appl. Surf. Sci. 158(1-2) (2000) 164–171.

[41] J.E. Berger, A.M. Jorge, Jr, G.Y. Koga, V. Roche, C.S. Kiminami, C. Bolfarini, W. J. Botta, Influence of chromium concentration and partial crystallization on the corrosion resistance of FeCrNiB amorphous alloys, Mater. Charact. 179 (2021) 111369.

[42] Y.Z. Ye, Z.J. Guo, Z.J. Zhou, B.S. Zhang, Q.Q. Wang, B.L. Shen, Improved corrosion and corrosion-wear properties of Fe-based high-entropy amorphous coatings by modulating heat input of HVAF, Corros. Sci. 232 (2024) 112049.

[43] C. Yang, H. Cai, S.H. Cui, J. Huang, J.Y. Zhu, Z.C. Wu, Z.Y. Ma, R.K.Y. Fu, L. Y. Sheng, X.B. Tian, P.K. Chu, Z.Z. Wu, A zinc-doped coating prepared on the magnesium alloy by plasma electrolytic oxidation for corrosion protection, Surf. Coat. Technol. 433 (2022) 128148.

[44] T.T. Thanaa, A. Fattah-alhosseini, M. Alkaseem, M. Kaseem, Improving the surface properties of Mg based-plasma electrolytic oxidation (PEO) coatings under the fluoride electrolytes: a review, Inorg. Chem. Commun. 170 (2024) 113163.

[45] M. Mohedano, E. Matykina, R. Arrabal, B. Mingo, A. Pardo, PEO of pre-anodized Al–Si alloys: corrosion properties and influence of sealings, Appl. Surf. Sci. 346 (2015) 57–67.

[46] Y. Zhao, H. Xiong, X.P. Li, W.L. Qi, J.D. Wang, Y. Hua, T. Zhang, F.H. Wang, Improved corrosion performance of selective laser melted stainless steel 316L in the deep-sea environment, Corros. Commun. 2 (2021) 55–62.

[47] A. Jangde, S. Kumar, C. Blawert, Influence of glycerol on plasma electrolytic oxidation coatings evolution and on corrosion behaviour of coated AM50 magnesium alloy, Corros. Sci. 157 (2019) 220–246.

[48] M. Toorani, M. Aliofkhazraei, M. Mahdavian, R. Naderi, Effective PEO/Silane pretreatment of epoxy coating applied on AZ31B mg alloy for corrosion protection, Corros. Sci. 169 (2020) 108608.

[49] X.M. Wang, L.Q. Zhu, X. He, F.L. Sun, Effect of cerium additive on aluminum-based chemical conversion coating on AZ91D magnesium alloy, Appl. Surf. Sci. 280 (2013) 467–473.

[50] H.H. Ryu, H.W. Lim, S.G. Lee, Y.K. Sun, Near-surface reconstruction in Ni-rich layered cathodes for high-performance lithium-ion batteries, Nat. Energy 9 (2024) 47–56.

[51] J. Jayaraj, S.Arun Kumar, A. Srinivasan, K.G. Raghu, C. Arunchandran, V. Rajinikanth, Corrosion and in vitro characteristics of cerium phosphate based chemical conversion coating on AZ31 magnesium alloy, Appl. Surf. Sci. 644 (2024) 158797.

[52] J.X. Gao, L.L. Tang, Z.Z. Shen, Y.M. Dong, Z.Y. Wang, J.Z. Lyu, J. Li, H.Q. Yu, Coupling of SiC and CeO2 nanosheets to enhance solar energy utilization and optimize catalytic ozonation, Appl. Catal. B Environ. 317 (2022) 121697.

[53] Y. Morozov, L.M. Calado, R.A. Shakoor, R. Raj, R. Kahraman, M.G. Taryba, M. F. Montemor, Epoxy coatings modified with a new cerium phosphate inhibitor for smart corrosion protection of steel, Corros. Sci. 159 (2019) 108128.

[54] M. Sowa, A. Olesinski, B. Szumski, A. Maciej, M. Bik, P. Jelen, M. Sitarz, W. Simka, Electrochemical characterization of anti-corrosion coatings formed on 6061 aluminum alloy by plasma electrolytic oxidation in the corrosion inhibitorenriched aqueous solutions, Electrochim. Acta 424 (2022) 140652.

[55] Y. Guo, A. Rogov, A. Hird, B. Mingo, A. Matthews, A. Yerokhin, Plasma electrolytic oxidation of magnesium by sawtooth pulse current, Surf. Coat. Technol. 429 (2022) 127938.

[56] Y.X. Wang, Y.K. Pan, X. Xu, W.D. Zhang, R. Feng, H. Li, Z.L. Gao, Improving corrosion and wear resistances of 2195 Al–Li alloy by PEO and LDHs composite coating, J. Mater. Res. Technol. 28 (2024) 1044–1061.

[57] M. Szkodo, A. Stanisławska, A. Komarov, Ł. Bolewski, Effect of MAO coatings on cavitation erosion and tribological properties of 5056 and 7075 aluminum alloys, Wear (2021) 474–475, 203709.

[58] M. Yıldırım, D. Ozyürek, The effects of Mg amount on the microstructure and mechanical properties of Al–Si–Mg alloys, Mater. Des. 51 (2013) 767–774.

[59] P. Deng, W.F. Mo, Z.Q. Ouyang, K. Ling, B.H. Luo, Z.H. Bai, Microstructural Evolution and Corrosion Mechanism of Micro-alloyed 2024 (Zr, Sc, Ag) Aluminum Alloys, Corros. Sci. 224 (2023) 111476.

[60] S. Gudić, I. Smoljko, M. KliskiC, The effect of small addition of tin and indium on the corrosion behavior of aluminium in chloride solution, J. Alloy. Compd. 505 (2010) 54–63.

[61] B. Zaid, D. Saidi, A. Benzaid, S. Hadji, Effects of pH and chloride concentration on pitting corrosion of AA6061 aluminum alloy, Corros. Sci. 50 (2008) 1841–1847.

[62] L.M. Caladoa, M.G. Taryba, Y. Morozov, M.J. Carmezim, M.F. Montemor, Novel smart and self-healing cerium phosphate-based corrosion inhibitor for AZ31 magnesium alloy, Corros. Sci. 170 (2020) 108648.

Supporting information

A self-sealing and self-healing MAO corrosion-resistant coating on aluminum alloy by *in situ* growth of $CePO_4/Al_2O_3$

Chao Yang [a], Zongmin Sun [a], Chenyu Wang [a], Aihui Huang [b,*], Zishuo Ye [c], Tao Ying [a], Liping Zhou [a], Shu Xiao [c,*], Paul K. Chu [d,*], Xiaoqin Zeng [a]

[a] National Engineering Research Center of Light Alloy Net Forming, School of Materials Science and Engineering, Shanghai Jiao Tong University, Shanghai, 200240, China

[b] Shanghai Key Laboratory of Advanced High-Temperature Materials and Precision Forming, School of Materials Science and Engineering, Shanghai Jiao Tong University, Shanghai, 200240, China

[c] School of Mechanical & Automotive Engineering, South China University of Technology, Guangzhou, 510641, China

[d] Department of Physics, Department of Materials Science & Engineering, and Department of Biomedical Engineering, City University of Hong Kong, Tat Chee Avenue, Kowloon, Hong Kong, 999077, China

∗ Corresponding authors:

E-mail addresses: huangaihuivip@sjtu.edu.cn (A.H. Huang); xiaos@scut.edu.cn (S. Xiao); paul.chu@cityu.edu.hk (P.K. Chu)

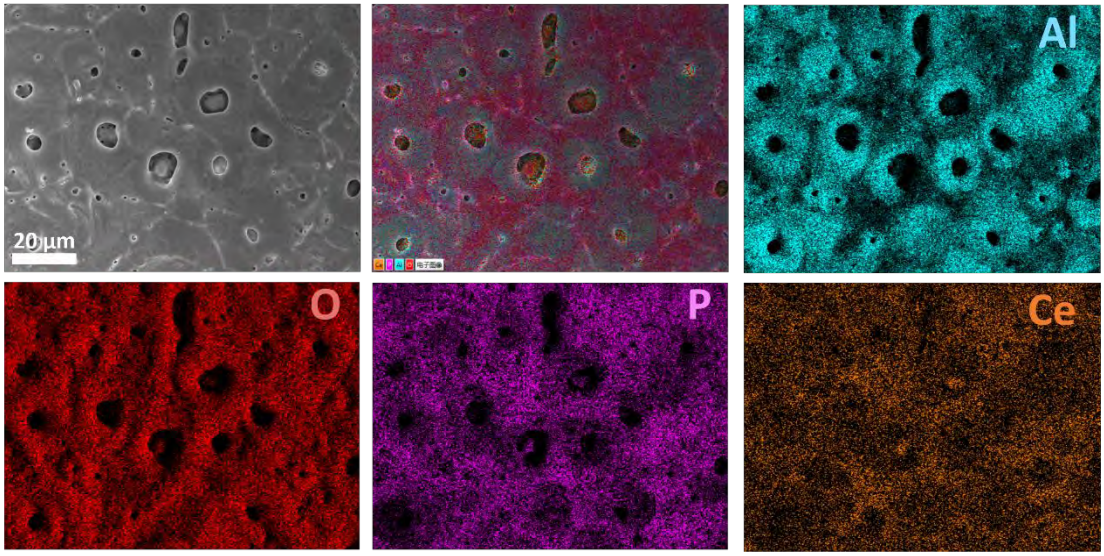

Fig. S1. SEM/EDS image and elemental maps of the Ce5 coating.

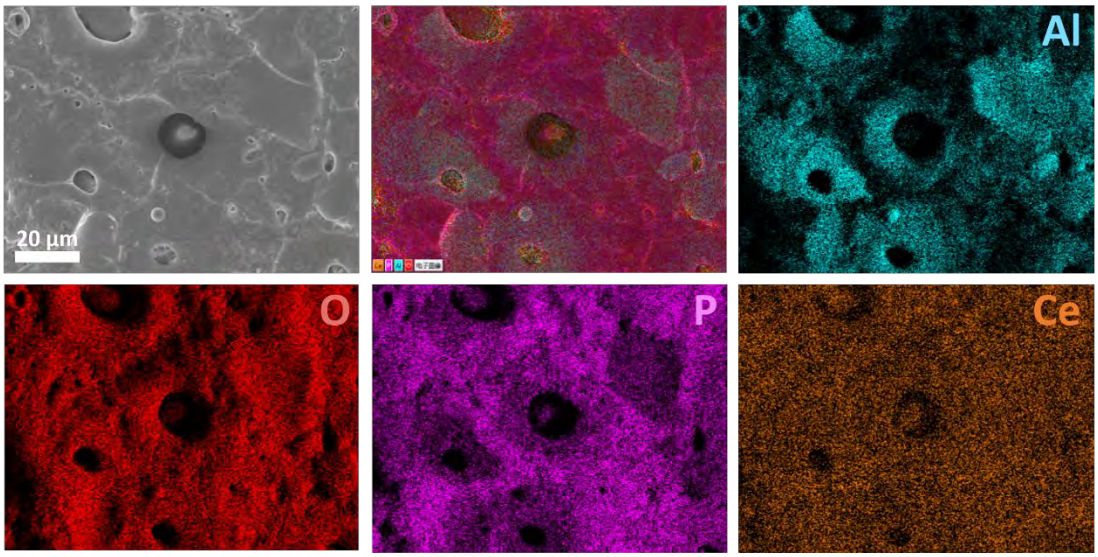

Fig. S2. SEM/EDS image and elemental maps of the Ce15 coating.

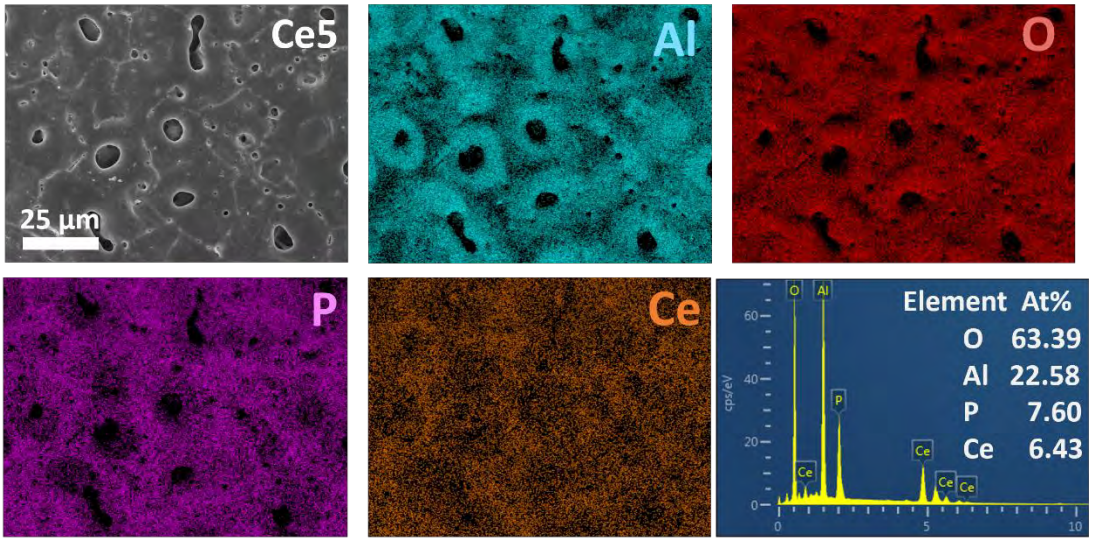

Fig. S3. SEM/EDS image, elemental maps, and spectrum of the Ce5 coating after immersion in a salt solution for 336 h.

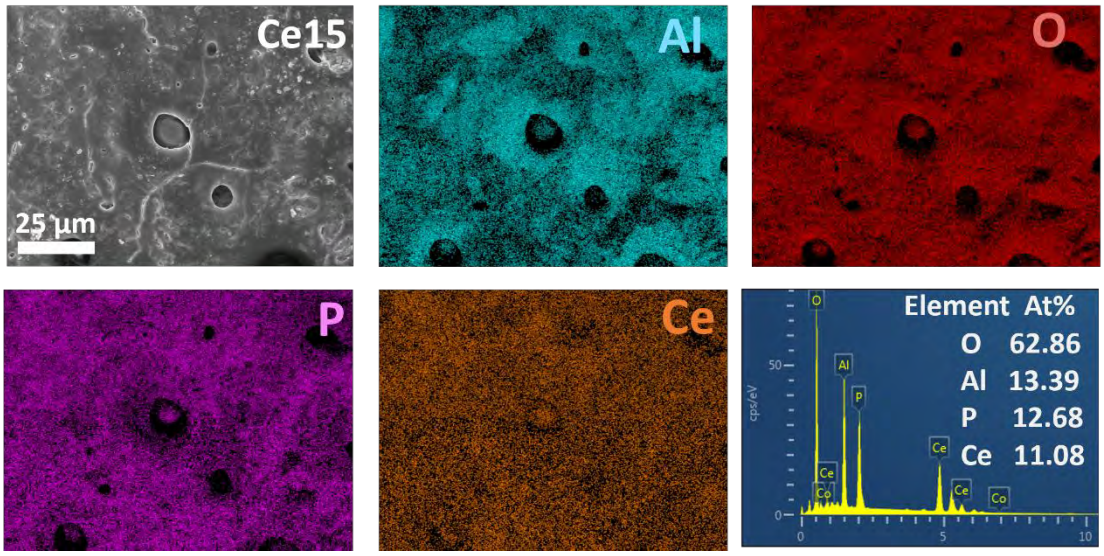

Fig. S4 SEM/EDS image, elemental maps, and spectrum of the Ce15 coating after immersion in a salt solution for 336 h.

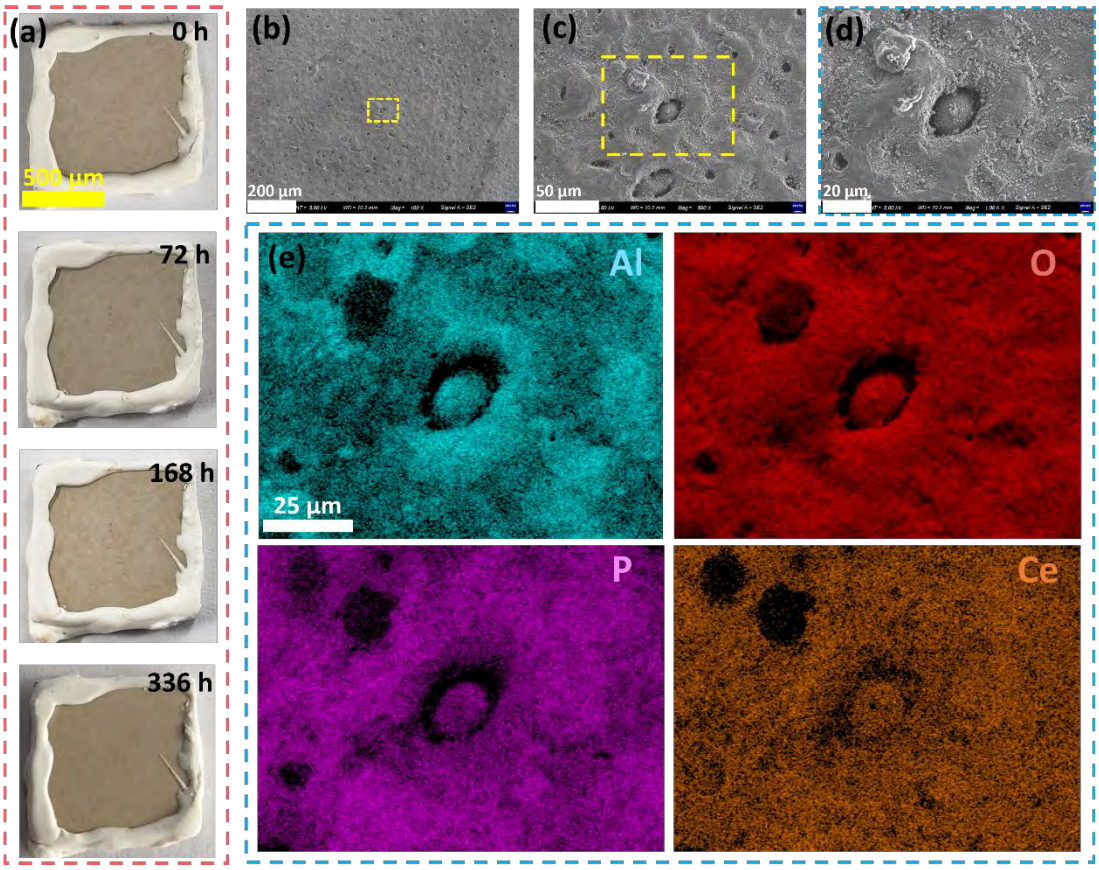

Fig. S5 Neutral salt spray corrosion results of Ce10 coating: (a) Optical images of coating at 0 h, 72 h, 168 h, and 336 h; (b-d) SEM image of coating at 336 h; (e) EDS results of (d).

Table S1. EIS result of the MAO coating after immersion in a salt solution for different time durations based on the EC.

Immersion time	1 h	48 h	168 h	336 h
R_s ($\Omega \cdot cm^2$)	32.3	30.5	30.8	34.6
CPE_p ($\Omega^{-1} \cdot cm^{-2} \cdot s^n$)	4.652×10^{-5}	9.127×10^{-5}	6.713×10^{-4}	5.212×10^{-3}
n_p	0.92	0.84	0.91	0.73
R_p ($\Omega \cdot cm^2$)	1.462×10^{3}	4.216×10^{2}	2.012×10^{2}	1.012×10^{2}
CPE_c ($\Omega^{-1} \cdot cm^{-2} \cdot s^n$)	5.252×10^{-6}	1.841×10^{-5}	7.542×10^{-5}	4.542×10^{-4}
n_c	0.77	0. 94	0.79	0.67
R_c ($\Omega \cdot cm^2$)	2.357×10^{4}	6.425×10^{3}	1.024×10^{3}	3.153×10^{2}
CPE_{dl} ($\Omega^{-1} \cdot cm^{-2} \cdot s^n$)	3.920×10^{-6}	9.262×10^{-6}	4.365×10^{-5}	2.612×10^{-4}
n_{dl}	0.87	0.80	0.76	0.91
R_{ct} ($\Omega \cdot cm^2$)	3.821×10^{4}	1.034×10^{4}	3.453×10^{3}	5.542×10^{2}
W($S \cdot sec^{0.5} \cdot cm^{-2}$)	—	—	—	—
L ($H \cdot cm^2$)	16.78	—	2.762×10^{3}	1.522×10^{3}
R_l ($\Omega \cdot cm^2$)	94.47	—	8.703×10^{3}	3.841×10^{3}
χ^2	3.3×10^{-4}	4.1×10^{-4}	2.9×10^{-3}	5.2×10^{-4}

Table S2 EIS results of the Ce5 coating after immersion in a salt solution for different time durations based on the EC.

Immersion time	1 h	48 h	168 h	336 h
R_s ($\Omega \cdot cm^2$)	29.5	31.6	29.9	32.1
CPE_p ($\Omega^{-1} \cdot cm^{-2} \cdot s^n$)	8.021×10^{-6}	3.716×10^{-5}	8.836×10^{-5}	5.721×10^{-4}
n_p	0.75	0.81	0.83	0.85
R_p ($\Omega \cdot cm^2$)	3.621×10^{4}	1.018×10^{4}	5.272×10^{3}	1.365×10^{3}
CPE_c ($\Omega^{-1} \cdot cm^{-2} \cdot s^n$)	8.321×10^{-7}	3.424×10^{-6}	9.736×10^{-6}	4.631×10^{-5}
n_c	0.82	0.89	0.99	0.98
R_c ($\Omega \cdot cm^2$)	2.234×10^{6}	1.022×10^{6}	5.832×10^{5}	1.006×10^{5}
CPE_{dl} ($\Omega^{-1} \cdot cm^{-2} \cdot s^n$)	6.321×10^{-7}	9.894×10^{-7}	5.836×10^{-6}	2.973×10^{-5}
n_{dl}	0.69	0.70	0.92	0.85
R_{ct} ($\Omega \cdot cm^2$)	1.681×10^{6}	5.335×10^{5}	1.276×10^{5}	7.392×10^{4}
W($S \cdot sec^{0.5} \cdot cm^{-2}$)	7.816×10^{-7}	3.812×10^{-6}	8.971×10^{-6}	3.861×10^{-5}
χ^2	4.2×10^{-3}	1.8×10^{-4}	3.7×10^{-3}	5.3×10^{-3}

Table S3. EIS result of the Ce10 coating after immersion in a salt solution for different time periods based on the EC.

Immersion time	1 h	48 h	168 h	336 h
R_s ($\Omega \cdot cm^2$)	30.2	30.7	30.5	29.8
CPE_p ($\Omega^{-1} \cdot cm^{-2} \cdot s^n$)	3.793×10^{-7}	5.821×10^{-7}	8.917×10^{-7}	4.715×10^{-6}
n_p	0.95	0.69	0.76	0.86
R_p ($\Omega \cdot cm^2$)	2.467×10^{5}	1.823×10^{5}	1.053×10^{5}	6.489×10^{4}
CPE_c ($\Omega^{-1} \cdot cm^{-2} \cdot s^n$)	5.235×10^{-8}	8.965×10^{-8}	3.614×10^{-7}	8.213×10^{-7}
n_c	0.88	0.91	0.86	0.74
R_c ($\Omega \cdot cm^2$)	6.132×10^{6}	4.022×10^{6}	2.683×10^{6}	6.356×10^{5}
CPE_{dl} ($\Omega^{-1} \cdot cm^{-2} \cdot s^n$)	3.659×10^{-8}	7.832×10^{-8}	1.097×10^{-7}	4.826×10^{-7}
n_{dl}	0.72	0.67	0.91	0.83
R_{ct} ($\Omega \cdot cm^2$)	3.254×10^{7}	2.172×10^{7}	6.541×10^{6}	1.645×10^{6}
W($S \cdot sec^{0.5} \cdot cm^{-2}$)	4.821×10^{-8}	7.816×10^{-8}	1.817×10^{-7}	6.751×10^{-7}
χ^2	2.9×10^{-4}	3.1×10^{-4}	6.2×10^{-3}	2.0×10^{-3}

Table S4. EIS result of the Ce15 coating after immersion in a salt solution for different time periods based on the EC.

Immersion time	1 h	48 h	168 h	336 h
R_s ($\Omega \cdot cm^2$)	32.4	29.7	29.8	30.8
CPE_p ($\Omega^{-1} \cdot cm^{-2} \cdot s^n$)	5.731×10^{-7}	9.216×10^{-7}	4.812×10^{-6}	8.998×10^{-6}
n_p	0.83	0.92	0.84	0.75
R_p ($\Omega \cdot cm^2$)	2.104×10^{5}	1.349×10^{5}	7.764×10^{4}	3.037×10^{4}
CPE_c ($\Omega^{-1} \cdot cm^{-2} \cdot s^n$)	7.127×10^{-8}	1.002×10^{-7}	4.765×10^{-7}	1.216×10^{-6}
n_c	0.62	0.94	0.83	0.81
R_c ($\Omega \cdot cm^2$)	5.862×10^{6}	3.654×10^{6}	1.227×10^{6}	3.616×10^{5}
CPE_{dl} ($\Omega^{-1} \cdot cm^{-2} \cdot s^n$)	4.621×10^{-8}	9.182×10^{-8}	3.733×10^{-7}	8.248×10^{-7}
n_{dl}	0.76	0.79	0.65	0.82
R_{ct} ($\Omega \cdot cm^2$)	2.874×10^{7}	1.126×10^{7}	3.244×10^{6}	7.896×10^{5}
W($S \cdot sec^{0.5} \cdot cm^{-2}$)	8.271×10^{-8}	3.861×10^{-7}	8.991×10^{-7}	3.716×10^{-6}
χ^2	2.6×10^{-4}	8.3×10^{-3}	9.1×10^{-3}	2.8×10^{-4}